

Fig. 2. In this work we examine equivalent circuits for the three oscillators. Each oscillator is composed of an LC tank, a negative conductance σ , and a nonlinear state-dependent current source $f(v_C, i_L)$.

sketched in Fig. 2 and conform to the aforementioned generic structure [32]. We rigorously characterize a variety of attributes for these oscillators including equilibria, small-signal stability, a notion of rise time, higher-order harmonic content, and oscillation frequency. The analytical developments are exhaustively verified with numerical simulations and experimental results wherein the oscillator dynamics underlie controllers for GFM inverters.

Our focus on perturbation and averaging is deliberate as it facilitates the translation of results to a broad class of nonlinear dynamical systems for which trajectories generated cannot be described in analytical closed form [33], [34]. In the context of the nonlinear circuits we examine, two particular attributes significantly facilitate analysis: 1) the vector fields that drive the oscillator amplitude and phase dynamics are periodic functions; 2) in the weakly nonlinear parametric regime where $\varepsilon = \sqrt{L/C} \ll 1$, the Van der Pol and dead-zone oscillators generate nearly sinusoidal trajectories. Larger values of ε yield so-called *relaxation* limit cycles [35]. (Interestingly, harmonic content in the Andronov-Hopf oscillator [36] is invariant to the choice of ε ; a property that we prove rigorously and one that is not immediately obvious from the dynamic model.) The combination of these two attributes allows us to apply averaging and perturbation to characterize the dynamics of these nonlinear oscillators. We provide a brief overview of these methodologies as follows.

- 1) Averaging involves integrating the driving vector fields under the presumption of operating in the weakly nonlinear regime. This isolates separable and autonomous models for amplitude and phase dynamics [37]. The averaged model allows us to characterize time-domain performance, equilibria, and small-signal stability.
- 2) Perturbation involves searching for solutions to the nonlinear dynamic models in the form of a power series where terms of increasing order diminish in size [38]. The idea being that while solutions to the original nonlinear models cannot be obtained analytically, order-by-order solutions for terms in the power series can be determined through a sequence of progressive substitutions and algebraic manipulations [39]. This allows us to parameterize the harmonic content and oscillation frequency.

TABLE I
CONTRIBUTIONS OF THIS ARTICLE (+); STATE OF THE ART (✓)

Oscillators	Van der Pol	Dead-zone	Andronov-Hopf
Models			
Cartesian	✓ [8], [40], [44]	✓ [11]	✓ [14]
Polar	✓ [8], [44]	+	✓ [14]
Circuit	✓ [8], [32], [44]	✓ [22]	+
Methods & Attributes			
Averaging			
• Equilibria	✓ [40], [44]	+	+
• Rise time	✓ [44]	+	+
• Experiments	✓ [45]	✓ [11]	+
Perturbation			
• Harmonics	✓ [44]	+	+
• Frequency	✓ [40]	+	+
• Experiments	✓ [44]	+	+

In addition to the choice of analytical methods, the collection of oscillators we examine is also intentional. The Van der Pol oscillator [40] undeniably enjoys unparalleled recognition as a prototypical example in introducing nonlinear dynamical systems [41]. This circuit, therefore, serves as a natural starting point and establishes the baseline in our effort. The dead-zone oscillator [42] generates waveforms that are superficially similar to the Van der Pol oscillator, but the piece-wise continuous nonlinearity [see Fig. 2(b)] introduces severe analytical obstacles to characterizing performance. To overcome the challenges associated with this circuit, we introduce a set of innovations within the conventional averaging and perturbation frameworks. Finally, the Andronov-Hopf oscillator [43] is unique in that the circuit always generates perfectly sinusoidal trajectories free of harmonics in steady state. Taken together, this trio of oscillators provides illustrative boundary cases for the averaging and perturbation methods and show the versatility of the proposed framework in performance characterization.

This article provides several analytical contributions through the process of applying averaging and perturbation to examine the dynamics of the Van der Pol, dead-zone, and Andronov-Hopf oscillators. For instance, the piece-wise continuous nonlinearity in the dead-zone oscillator is incompatible with perturbation methods. This is circumvented by resorting to a Fourier-series expansion of the nonlinearity and incorporating the resulting terms alongside the series expansion in the perturbation analysis. We anticipate this general strategy being useful in other circuits that have similar discontinuities in their dynamic models; a well-known example is Chua's circuit [46]. Furthermore, to the extent possible, our analytical examinations are presented in a unified manner and this uncovers several cross-cutting links. For instance, boundary conditions that emerge from the perturbation analysis yield expressions for equilibrium amplitudes that precisely match those recovered from a steady-state analysis of the oscillator averaged dynamics. By and large, the article unifies models (Cartesian, polar, and circuit representations), methods (averaging and perturbation), and attributes (dynamic and harmonic). Table I provides an overview of the contributions of this article alongside the state-of-the-art for the three oscillators with

regard to modeling formalisms, applied methods, and examined attributes. After outlining foundational theory, we then analyze the impact of current feedback on system dynamics and provide an associated design framework that respects user-defined performance metrics. As evidenced in the experimental results, this allows us to translate fundamental modeling advances into practical design and hardware implementations.

The rest of this article is organized as follows. In Section II, modeling and analysis preliminaries are covered. Averaging and perturbation theory are outlined in Sections III and IV to characterize amplitude dynamics and steady-state frequency content, respectively. Section V provides an analysis of voltage and frequency dynamics in the presence of current feedback in a practical power electronics setting. This also lays the groundwork for a design framework. Once relevant performance metrics are in hand, they are validated in Section VI for the Van der Pol, dead-zone, and Andronov-Hopf oscillators via simulations and experiments. In addition, a multiinverter power system is built to substantiate the performance of the Andronov-Hopf oscillator. Finally, Section VII concludes this article.

II. MODELS AND CIRCUIT REPRESENTATIONS

In this section, we outline dynamic models for the three oscillators in Cartesian and polar coordinates as well as circuit representations. Table II collects pertinent dynamic and harmonic attributes of all three oscillator models in one place. It primarily serves as a quick reference guide and the derivations later will substantiate its content.^{1,2}

A. Dynamic Model in Cartesian Coordinates

The oscillator dynamics in Cartesian coordinates are

$$\dot{x} = \varepsilon \omega_0 (\sigma x - f(x, y)) - \omega_0 y \quad (1a)$$

$$\dot{y} = \omega_0 x \quad (1b)$$

where x, y are state variables, $\omega_0 > 0$ is the natural frequency and $\sigma, \varepsilon > 0$ are scalar constants.

Notice that ε captures the extent to which the *nonlinear* function $f(x, y)$ affects system dynamics; with $\varepsilon = 0$, (1) boils down to the dynamics of a simple harmonic oscillator. The dynamics of x and y are interdependent, and the nonlinear coupling through $f(x, y)$ serves up several analytical challenges. In this work, we are interested in the *weakly nonlinear* regime characterized by $\varepsilon \ll 1$ [41]. As we develop circuit interpretations going forward, we will show that $f(x, y)$ can be thought of as a single-port dissipative circuit element and σ has the connotation of a conductance. The dynamics (1) can be equivalently expressed as the second-order system

$$\ddot{x} + 2\zeta(x, y)\omega_0\dot{x} + \omega^2(x, y)x = 0 \quad (2)$$

where $y(t) = \omega_0 \int x dt$ [see (1b)], and $\zeta(x, y)$ and $\omega(x, y)$ are referred to as the *generalized-damping* and *generalized-frequency*

functions, respectively. These are given by

$$\zeta(x, y) := \frac{\varepsilon}{2} \left(\frac{\partial f}{\partial x} - \frac{x}{y} \frac{\partial f}{\partial y} - \sigma \right) \quad (3)$$

$$\omega(x, y) := \omega_0 \left(1 + \varepsilon^2 \frac{\sigma x - f(x, y)}{y} \frac{\partial f}{\partial y} \right)^{\frac{1}{2}}. \quad (4)$$

See Appendix A for the derivation. The form (2) is reminiscent of a classical unforced second-order oscillator [47]. Key differences are that the damping and frequency factors are now expressed as time-varying and state-dependent functions.

B. Dynamic Model Interpreted as a Circuit

The building block of the circuit representation is an electrical LC tank with inductance L and capacitance C . Denote the inductor current and capacitor voltage as i_L and v_C , respectively. From Fig. 2, we get the following model:

$$C\dot{v}_C = -i_L - f(v_C, i_L) + \sigma v_C \quad (5a)$$

$$L\dot{i}_L = v_C \quad (5b)$$

with the definition $x = v_C$ and $y = \varepsilon i_L$, and $\varepsilon = \sqrt{L/C}$ denoting the *characteristic impedance* of the LC tank. Furthermore $\omega_0 = \sqrt{1/LC}$ is the *natural frequency* of the LC tank. The right-hand sides of (5a) and (5b) act as instances of the Kirchhoff's current and voltage laws, respectively, and yield the circuit models in Fig. 2. The nonlinear function $f(v_C, i_L)$ (which is different for each oscillator) is a state-dependent current source that *absorbs* power $f(v_C, i_L) \times v_C \geq 0$. By contrast, $-\sigma$ is a negative conductance, which *produces* power $v_C^2 \times \sigma \geq 0$. In summary, $f(v_C, i_L)$ and σ are single-port dissipative and nondissipative elements, respectively, and they complete the circuit representation along with the LC tank. See Appendix B for a derivation of how the model in (1) follows from (5).

C. Dynamic Model in Polar Coordinates

We now derive polar-coordinate models for the oscillator dynamics. These will be key to quantify voltage amplitude, frequency, and other harmonic properties when the oscillator dynamics are deployed as controllers for the inverters. To derive the polar coordinates model, we consider the following projection of states x and y (i.e., v_C and εi_L):

$$x = r \cos \theta, \quad y = r \sin \theta \quad (6)$$

where r and θ are the instantaneous amplitude and phase, respectively. Notice that the instantaneous phase is defined without any anchor to a rotating reference frame. The inverse of the transformation is given by

$$r = \sqrt{x^2 + y^2}, \quad \theta = \tan^{-1} \left(\frac{y}{x} \right).$$

With these definitions in place, the dynamics of r and θ for the unforced oscillator dynamics are

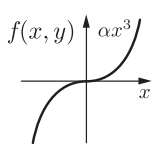
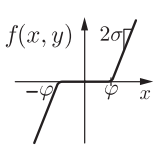
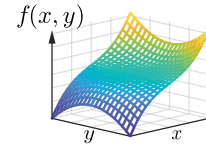
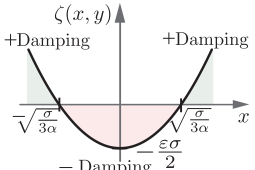
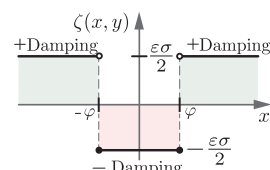
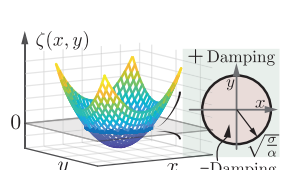
$$\dot{r} = \varepsilon \omega_0 (\sigma r \cos \theta - f(r \cos \theta, r \sin \theta)) \cos \theta \quad (7a)$$

$$\dot{\theta} = \omega_0 - \varepsilon \omega_0 \left(\sigma \cos \theta - \frac{f(r \cos \theta, r \sin \theta)}{r} \right) \sin \theta. \quad (7b)$$

¹ All decimal numerical values are specified with three significant digits.

² Values of $\theta_1, \dots, \theta_4$ referenced in (15) and (18) are given in (34).

TABLE II
 SUMMARY OF MODELS AND KEY FINDINGS FOR THE NONLINEAR OSCILLATORS

	Van der Pol oscillator	Dead-zone oscillator	Andronov-Hopf oscillator
$f(x, y)$	αx^3 (8) 	$\begin{cases} 2\sigma(x - \varphi), & x > \varphi \\ 0, & -\varphi \leq x \leq \varphi \\ 2\sigma(x + \varphi), & x < -\varphi. \end{cases}$ (9) 	$\alpha(x^2 + y^2)x$ (10) 
$\zeta(x, y)$	$\frac{\varepsilon}{2}(3\alpha x^2 - \sigma)$ (11) 	$\begin{cases} +\frac{\varepsilon\sigma}{2}, & x < -\varphi \parallel x > \varphi \\ -\frac{\varepsilon\sigma}{2}, & -\varphi \leq x \leq \varphi. \end{cases}$ (12) 	$\frac{\varepsilon}{2}(\alpha(x^2 + y^2) - \sigma)$ (13) 
$\omega(x, y)$	ω_0	ω_0	$\omega_0(1 + 2\varepsilon^2\alpha x^2(\sigma - \alpha(x^2 + y^2)))$
$\frac{\dot{r}}{\varepsilon\sigma\omega_0}$	$r \cos^2 \theta \left(1 - \frac{\alpha}{\sigma} r^2 \cos^2 \theta\right)$ (14)	i) $r < \varphi$: $r \cos^2 \theta$ ii) $r \geq \varphi$: $\begin{cases} -r \cos^2 \theta + 2\varphi \cos \theta, & [\theta_4 - 2\pi, \theta_1) \\ r \cos^2 \theta, & (\theta_1, \theta_2] \cup [\theta_3, \theta_4) \\ -r \cos^2 \theta - 2\varphi \cos \theta, & (\theta_2, \theta_3]. \end{cases}$ (15)	$\frac{r}{2} \left(1 - \frac{\alpha}{\sigma} r^2\right)$ (16)
$\frac{\dot{\theta} - \omega_0}{\varepsilon\sigma\omega_0}$	$\frac{\sin 2\theta}{2} \left(\frac{\alpha r^2}{\sigma} \cos^2 \theta - 1\right)$ (17)	i) $r < \varphi$: $-\sin \theta \cos \theta$ ii) $r \geq \varphi$: $\begin{cases} \sin \theta \cos \theta - \frac{2\varphi}{r} \sin \theta, & [\theta_4 - 2\pi, \theta_1) \\ -\sin \theta \cos \theta, & (\theta_1, \theta_2] \cup [\theta_3, \theta_4) \\ \sin \theta \cos \theta + \frac{2\varphi}{r} \sin \theta, & (\theta_2, \theta_3]. \end{cases}$ (18)	$\frac{\sin 2\theta}{2} \left(\frac{\alpha r^2}{\sigma} - 1\right)$ (19)
$\frac{g(\bar{r})}{\varepsilon\sigma\omega_0}$	$\frac{\bar{r}}{8} \left(4 - \frac{3\alpha}{\sigma} \bar{r}^2\right)$ (20)	$\begin{cases} \frac{\bar{r}}{2}, & (\bar{r} \leq \varphi) \\ \frac{2\bar{r}}{\pi} \left(\frac{\varphi\sqrt{\bar{r}^2 - \varphi^2}}{\bar{r}^2} - \cos^{-1}\left(\frac{\varphi}{\bar{r}}\right) + \frac{\pi}{4}\right), & (\bar{r} > \varphi) \end{cases}$ (21)	$\frac{\bar{r}}{2} \left(1 - \frac{\alpha}{\sigma} \bar{r}^2\right)$ (22)
\bar{r}_{eq}	$2\sqrt{\sigma/3\alpha}$ (23)	2.48φ (24)	$\sqrt{\sigma/\alpha}$ (25)
t_{rise}	$\frac{6}{\varepsilon\sigma\omega_0}$ (26)	$\frac{6.84}{\varepsilon\sigma\omega_0}$ (27)	$\frac{6}{\varepsilon\sigma\omega_0}$ (28)
γ_3	$\frac{\varepsilon\sigma}{8}$ (29)	$\frac{0.788\varepsilon\sigma}{8}$ (30)	0
ω_{eq}	$\left(1 - \frac{\varepsilon^2\sigma^2}{16}\right)\omega_0$ (31)	$\left(1 - \frac{0.690\varepsilon^2\sigma^2}{16}\right)\omega_0$ (32)	ω_0 (33)

From the abovementioned equations, we observe that the oscillation frequency $\omega = \dot{\theta}$ is state dependent and distinct from the natural frequency ω_0 . However, in the weakly nonlinear region, $\varepsilon \ll 1$, we can see that: 1) $\dot{r} \ll \dot{x}$ or \dot{y} , the amplitude r evolves slower than states x, y , and 2) the oscillation frequency $\omega = \dot{\theta} \approx \omega_0$. We leverage these observations to obtain a separable and autonomous version of the amplitude dynamics via averaging in Section III.

D. Oscillator Models and Some Takeaways

Having established dynamical models in the Cartesian and polar coordinates as well as suitable circuit interpretations, we now examine distinguishing features for each oscillator.

1) *Van Der Pol Oscillator*: The nonlinearity takes the form $f(x, y) = \alpha x^3$, where $\alpha > 0$ is a constant. Using (3), we obtain the damping function in (11). As illustrated in Table II, this is parabolic and depends only on state x . When x is small, the nondissipative σ term in (11) dominates and $\zeta(x, y) < 0$ implies negative damping that builds up the states. As x grows (and breaches the boundary defined by $3\alpha x^2 = \sigma$), we obtain positive damping that opposes further growth. Since $f(x, y)$ only depends on x , $\partial f / \partial y = 0$, and $\omega(x, y) = \omega_0$. The equivalent circuit of the Van der Pol oscillator is illustrated in Fig. 2(a). This representation finds frequent mention in the literature as a motivating example for nonlinear circuits [41].

2) *Dead-Zone Oscillator*: This oscillator is characterized by the nonlinearity in (9), where φ is a positive constant. The generalized damping function is given by (3) and illustrated in Table II. Note that the damping is a discontinuous piece-wise constant function. In the regime $-\varphi \leq x \leq \varphi$, we have negative damping such that energy is injected into the LC tank, while larger values of x are associated with positive damping that curtails growth. As with the Van der Pol oscillator, $\partial f / \partial y = 0$, and $\omega(x, y) = \omega_0$. The amplitude dynamics in polar coordinates are reported in (15). Since $f(\cdot, \cdot)$ is piece-wise linear, we get three dynamical-system descriptions over the interval $[0, 2\pi)$. The breakpoints $\theta_1, \dots, \theta_4$ are given by

$$\begin{aligned} \theta_1 &= \cos^{-1} \frac{\varphi}{r}, & \theta_2 &= \pi - \cos^{-1} \frac{\varphi}{r} \\ \theta_3 &= \pi + \cos^{-1} \frac{\varphi}{r}, & \theta_4 &= 2\pi - \cos^{-1} \frac{\varphi}{r}. \end{aligned} \quad (34)$$

[See Fig. 3(b) for an illustration.]

3) *Andronov-Hopf Oscillator*: This oscillator is characterized by the function $f(x, y) = \alpha(x^2 + y^2)x$, where $\alpha > 0$ is a constant [48]. Compared to the Van der Pol oscillator, the $f(x, y)$ has an additional $\alpha y^2 x$ term. The generalized damping function $\zeta(x, y)$ is given in (13) and illustrated in Table II, from which we observe the function to be a paraboloid. When trajectories lie outside (inside) the circle with radius $\sqrt{\sigma/\alpha}$, the damping is positive (negative, respectively). This generates a stable limit cycle $x^2 + y^2 = \sigma/\alpha$ and in periodic steady state we get evolution constrained to the surface characterized by $\sigma x - f(x, y) = 0$ and $\omega(x, y) = \omega_0$. Interestingly, we note that $f(\cdot, \cdot)$ and $\zeta(\cdot, \cdot)$ collapse to that of the Van der Pol oscillator for $y = 0$.

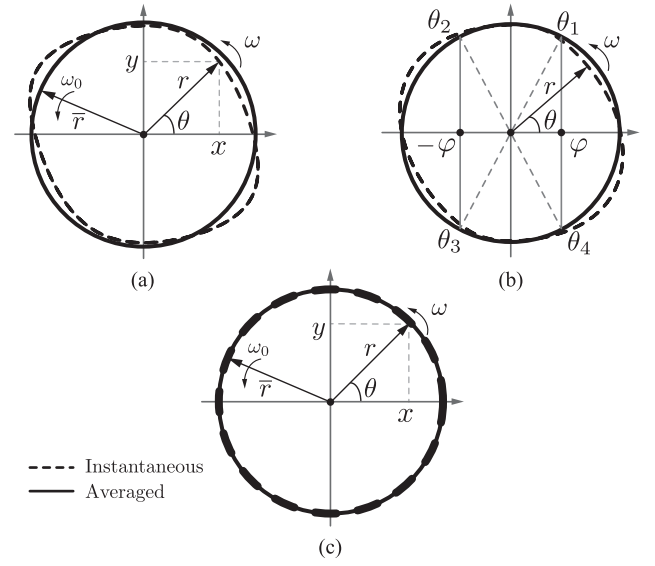


Fig. 3. Trajectories of instantaneous and averaged dynamics in the weakly nonlinear regime, $\varepsilon \ll 1$, illustrated for the (a) Van der Pol, (b) dead-zone oscillators, and (c) Andronov-Hopf oscillator. Differences in r and \bar{r} are exaggerated for emphasis.

Remark 1: The nonlinear and coupled nature of the oscillator dynamics (in both the Cartesian and polar forms) preclude the analytical determination of attributes, such as steady-state equilibria, stability of generated limit cycles, higher-order harmonic content, and oscillation frequency. However, two observations are particularly useful in this regard: 1) the amplitude and phase dynamics (7) are 2π periodic in θ ; 2) in the weakly nonlinear regime $\varepsilon \ll 1$, we recognize that (1) should yield nearly sinusoidal trajectories that evolve with frequency close to ω_0 . The combination of these will, in fact, be useful in isolating the amplitude dynamics and characterizing harmonic content in the trajectories.

We tackle time-domain performance, steady-state equilibria, and small-signal stability in Section III by suitably isolating a tractable model for amplitude dynamics under the supposition that limit cycles generated in the parametric regime $\varepsilon \ll 1$ evolve close to natural frequency ω_0 . Following this, in Section IV we characterize harmonics by searching for solutions to (2) expressed as a series expansion in harmonic terms.

III. AVERAGING ANALYSIS: EQUILIBRIA, STABILITY, AND DYNAMIC PERFORMANCE

To characterize periodic steady-state equilibria and dynamic performance, we turn to averaging theory [37]. This approach uncovers an analytically tractable—albeit *approximate*—model for amplitude dynamics from (7a). After a brief overview of averaging, we analyze the three oscillators individually. In this section, we first study oscillators with no current feedback (i.e., we suppose $\kappa_i = 0$ in Fig. 1). Voltage dynamics under nonzero current feedback will be studied subsequently in Section V.

A. Fundamentals of Averaging

We begin with the polar coordinates model for amplitude in (7a), and average the driving dynamics over one period

$$\dot{\bar{r}} = \frac{1}{2\pi} \int_{\theta=0}^{2\pi} \varepsilon \omega_0 (\sigma \bar{r} \cos \theta - f(\bar{r} \cos \theta, \bar{r} \sin \theta)) \cos \theta d\theta. \quad (35)$$

Note that the cycle-average amplitude that results from this model is denoted by \bar{r} . In the weakly nonlinear regime, $\varepsilon \ll 1$, it can be shown that over the timescale $\omega_0 t$, the error induced by the averaging approximation $|\bar{r}(t) - r(t)|$ is $\mathcal{O}(\varepsilon)$ [37]. Following the same approach as the ones mentioned above, we average the phase dynamics in (7b) to obtain

$$\dot{\bar{\theta}} = \frac{\omega_0}{2\pi} \int_{\theta=0}^{2\pi} 1 - \varepsilon \left(\sigma \cos \theta - \frac{f(r \cos \theta, r \sin \theta)}{r} \right) \sin \theta d\theta. \quad (36)$$

For all three oscillators, it happens that the one mentioned above boils down to $\dot{\bar{\theta}} = \omega_0$. This demonstrates alignment with the underlying premise of averaging, which is based on the premise of weakly nonlinear dynamics that oscillates near the natural frequency. See related discussion as follows (7b).

B. Small-Signal Stability of Equilibria and Rise Time

In what follows, we will show that the averaged amplitude dynamics for all three oscillators takes the form

$$\dot{\bar{r}} = g(\bar{r}). \quad (37)$$

The functions $g(\bar{r})$ for the three oscillators are listed in (20)–(22) (see also, Fig. 3). The derivation for the dead-zone oscillator requires additional manipulations given its piece-wise continuous amplitude vector field (15) (details are reported in Appendix A). Notably, (37) is autonomous (i.e., there is no dependence on $\bar{\theta}$) and variable separable (i.e., $g(\cdot)$ does not explicitly depend on time). Given the averaged amplitude dynamics, we focus on steady-state equilibria and dynamic performance. Since the dynamics of the oscillators are nonlinear, it is important to get a clear understanding of all possible equilibria that may result when they are deployed as controllers for inverters. In this spirit, we isolate all possible equilibria and conclusively establish that high-voltage and nonzero equilibria in each case are small-signal stable. Equilibria, \bar{r}_{eq} , are obtained from solving the algebraic constraint $g(\bar{r}_{\text{eq}}) = 0$. Small-signal stability of equilibria is evaluated by considering the linearized dynamics of $\Delta \bar{r} := \bar{r} - \bar{r}_{\text{eq}}$. This takes the form

$$\Delta \dot{\bar{r}} = \left. \frac{\partial}{\partial \bar{r}} g(\bar{r}) \right|_{\bar{r}=\bar{r}_{\text{eq}}} \Delta \bar{r}. \quad (38)$$

The averaged amplitude \bar{r} is exponentially stable around the equilibrium point \bar{r}_{eq} if and only if $\partial g(\bar{r}_{\text{eq}})/\partial \bar{r} < 0$.

With regard to dynamic performance, we focus on a notion of rise time t_{rise} defined to be the time for the averaged amplitude to build up from 10% to 90% of \bar{r}_{eq} . This can be computed from (37) as

$$t_{\text{rise}} = \int_{\bar{r}=0.1\bar{r}_{\text{eq}}}^{0.9\bar{r}_{\text{eq}}} \frac{1}{g(\bar{r})} d\bar{r}. \quad (39)$$

The abovementioned limits are chosen without the loss of generality. In particular, inferences on dynamic performance that we make subsequently would apply equivalently to other limits as well.

C. Dynamic Properties of Oscillators

The following analysis establishes equilibria, small-signal stability, and rise time for each oscillator.

1) *Van Der Pol Oscillator*: The stationary points of the averaged amplitude dynamics in (20) reveal equilibria at $0, \pm \sqrt{2\sigma/3\alpha}$. The linearized amplitude dynamics around the equilibrium \bar{r}_{eq} can be obtained based on (38) as

$$\Delta \dot{\bar{r}} = \varepsilon \sigma \omega_0 \left(\frac{1}{2} - \frac{9\alpha}{8\sigma} \bar{r}_{\text{eq}}^2 \right) \Delta \bar{r} \quad (40)$$

from which it follows that the equilibrium in (23) is small-signal stable. Finally, applying (39) gives the rise time in (26).

2) *Dead-Zone Oscillator*: Linearizing the averaged amplitude dynamics in (21) yields

$$\Delta \dot{\bar{r}} = \varepsilon \sigma \omega_0 \left(\frac{\pi}{2} - 2 \cos^{-1} \left(\frac{\varphi}{\bar{r}_{\text{eq}}} \right) \right) \bar{r}_{\text{eq}} \Delta \bar{r}. \quad (41)$$

Numerically evaluating fixed points of (21) that satisfy the small-signal stability constraint

$$\frac{\pi}{2} - 2 \cos^{-1} \left(\frac{\varphi}{\bar{r}_{\text{eq}}} \right) < 0$$

gives the equilibrium amplitude reported in (24). The rise time for the dead-zone oscillator is given in (27). Note that this computation involves some detailed algebra due to the trigonometric nonlinearity in the amplitude dynamics. (See Appendix B for details.)

3) *Andronov-Hopf Oscillator*: Stationary points of (22) reveal equilibria at $0, \pm \sqrt{\frac{\sigma}{\alpha}} \kappa_v$. The linearized amplitude dynamics are given by

$$\Delta \dot{\bar{r}} = \varepsilon \sigma \omega_0 \left(\frac{1}{2} - \frac{3\alpha}{2\sigma} \bar{r}_{\text{eq}}^2 \right) \Delta \bar{r} \quad (42)$$

from which, we can conclude that the equilibrium amplitude in (25) is small-signal stable. The rise time for this oscillator is noted in (28).

Remark 2: From (26) to (28), we can conclude that dynamic performance, captured by rise time, is inversely proportional to the product $\varepsilon \sigma$ for all three oscillators. In what follows, we will establish that harmonic content is directly proportional to $\varepsilon \sigma$ for the Van der Pol and dead-zone oscillators. This establishes a tradeoff and precludes selecting arbitrarily large values of ε, σ in an attempt to prioritize dynamic performance. We formalize the process of parameter selection in Section V.

IV. PERTURBATION THEORY: ESTIMATING HARMONIC CONTENT AND OSCILLATION FREQUENCY

We first provide a brief primer on perturbation theory [37], and in particular, the Poincaré-Lindstedt method. Following this, we apply the method to estimate third-to-fundamental harmonic

content and the steady-state oscillation frequency for all three oscillators.

A. Fundamentals of Perturbation Theory

Consider the second-order oscillator model in (2). Since $\omega(x, y) = \omega_0$ in periodic steady state for all three oscillators, this model simplifies to

$$\ddot{x} + 2\zeta(x, y)\omega_0\dot{x} + \omega_0^2 x = 0. \quad (43)$$

We introduce a new timescale $\tau = \omega_{\text{eq}} t$ to facilitate analysis, where ω_{eq} is the equilibrium oscillation frequency defined in the context of (7b) by

$$\omega_{\text{eq}} := \lim_{t \rightarrow \infty} \dot{\theta}(t). \quad (44)$$

Remark 3: We make the distinction between the generalized-frequency function $\omega(x, y)$ in (4), the actual oscillation frequency $\dot{\theta} = \omega$ in (7b), the natural frequency of oscillation ω_0 and the equilibrium oscillation frequency ω_{eq} , defined in (44). In particular, the actual frequency of oscillation $\dot{\theta}$ with steady-state value ω_{eq} (see (31)–(33) for the three oscillators) is not equal to ω_0 .

Henceforth, the first- and second-order derivatives of x with respect to the new timescale τ are denoted by x' and x'' , respectively. These are defined as

$$x' = \frac{dx}{d\tau} = \frac{dt}{d\tau} \frac{dx}{dt} = \omega_{\text{eq}}^{-1} \dot{x}, \quad x'' = \omega_{\text{eq}}^{-2} \ddot{x}. \quad (45)$$

Then, the system in (43) can be expressed as

$$\omega_{\text{eq}}^2 x'' + 2\zeta(x, y)\omega_0\omega_{\text{eq}}x' + \omega_0^2 x = 0 \quad (46)$$

where $y(\tau) = \omega_0\omega_{\text{eq}}^{-1} \int x(\tau) d\tau$.

The coupled and nonlinear phase-dynamics model in (7b) lacks a closed-form analytical solution for ω_{eq} . (Recall that the same was true in the case of the amplitude dynamics, and we resorted to averaging as a workaround.) In what follows, we express the equilibrium frequency (with a slight abuse of notation) as the series

$$\omega_{\text{eq}} = \sum_{k=0}^{\infty} \epsilon^k \omega_k \quad (47)$$

where ω_0 is the natural frequency [introduced previously in (1)] and $\epsilon = \varepsilon\sigma$ is a small dimensionless scalar.³ Mirroring the series expansion for equilibrium frequency, we seek solutions to (46) of the general series-expansion form

$$x(\tau) = \sum_{k=0}^{\infty} \epsilon^k x_k(\tau). \quad (48)$$

We will utilize a scaled version of the generalized damping function given by

$$\hat{\zeta}(x, y) = \frac{1}{\epsilon} \zeta(x, y) \quad (49)$$

³To see this, consider the circuit representation wherein ε is the characteristic impedance of the LC tank and σ is a conductance. Therefore, the product, $\varepsilon\sigma = \epsilon$, is dimensionless.

for developments that follow.

We will adopt a similar series expansion as in (47) and (48) for $\hat{\zeta}(x, y)$, as well as a first-order Taylor-series approximation around (x_0, y_0) to facilitate computations⁴

$$\begin{aligned} \hat{\zeta}(x, y) &= \sum_{k=0}^{\infty} \epsilon^k \hat{\zeta}_k \\ &= \hat{\zeta}(x_0, y_0) + \epsilon \left(x_1 \frac{\partial \hat{\zeta}(x_0, y_0)}{\partial x} + y_1 \frac{\partial \hat{\zeta}(x_0, y_0)}{\partial y} \right). \end{aligned} \quad (50)$$

Equating coefficients of same order ϵ yields

$$\hat{\zeta}_0 = \hat{\zeta}(x_0, y_0), \quad \hat{\zeta}_1 = x_1 \frac{\partial \hat{\zeta}(x_0, y_0)}{\partial x} + y_1 \frac{\partial \hat{\zeta}(x_0, y_0)}{\partial y}. \quad (51)$$

Since $\hat{\zeta}(x, y)$ depends only on x for the Van der Pol and dead-zone oscillators, $\partial \hat{\zeta}(x, y) / \partial y = 0$ in (51) for these circuits.

B. Equilibrium Frequency and Harmonic Content

Substituting (47)–(50) into (46) and collecting terms of the same order ϵ , we get following expressions up to second order:

$$\mathcal{O}(1) : x''_0 + x_0 = 0 \quad (52a)$$

$$\mathcal{O}(\epsilon) : x''_1 + x_1 = -\frac{2\omega_1}{\omega_0} x''_0 - 2\hat{\zeta}_0 x'_0 \quad (52b)$$

$$\begin{aligned} \mathcal{O}(\epsilon^2) : x''_2 + x_2 &= -\frac{2\omega_1}{\omega_0} x''_1 - \frac{2\omega_2}{\omega_0} x''_0 - \frac{\omega_1^2}{\omega_0^2} x''_0 \\ &\quad - 2\hat{\zeta}_0 x'_1 - 2\frac{\omega_1}{\omega_0} \hat{\zeta}_0 x'_0 - 2\hat{\zeta}_1 x'_0. \end{aligned} \quad (52c)$$

Notice that x_k for $k = 0, 1, 2$ can be solved in a sequential order-by-order fashion. First, we recognize that (52a) corresponds to the dynamics of a classic unforced second-order harmonic oscillator with solution expressed as $x_0 = \chi \cos \tau$, where $\chi > 0$ is a constant that depends on the initial conditions. Next, note that $\omega_1 = 0$. If this were not the case, the solution for (52b) may contain secular terms of the form $\tau \sin \tau$ and $\tau \cos \tau$ that grow without bound. This would turn up several contradictions, e.g., it would violate the small-signal stability of amplitude equilibria established in Section III. These observations allow us to simplify (52b) as

$$x''_1 + x_1 = 2\hat{\zeta}_0 \chi \sin \tau. \quad (53)$$

With $\hat{\zeta}_0$ in hand from (51), the solution of (53) yields x_1 and $\hat{\zeta}_1$. The ratio of third-to-fundamental harmonic content in x_1 to χ is denoted by γ_3 ; this is one key harmonic attribute that will be computed for all three oscillators. Finally, substituting $\omega_1 = 0$ in (52c) yields

$$x''_2 + x_2 = 2\frac{\omega_2}{\omega_0} \chi \cos \tau - 2\hat{\zeta}_0 x'_1 - 2\hat{\zeta}_1 x'_0. \quad (54)$$

⁴We will find that a first-order Taylor-series approximation is sufficient to approximate equilibrium frequency to second order, and to quantify harmonic content to third order. Higher-order harmonic analysis would correspondingly require higher-order Taylor-series expansions.

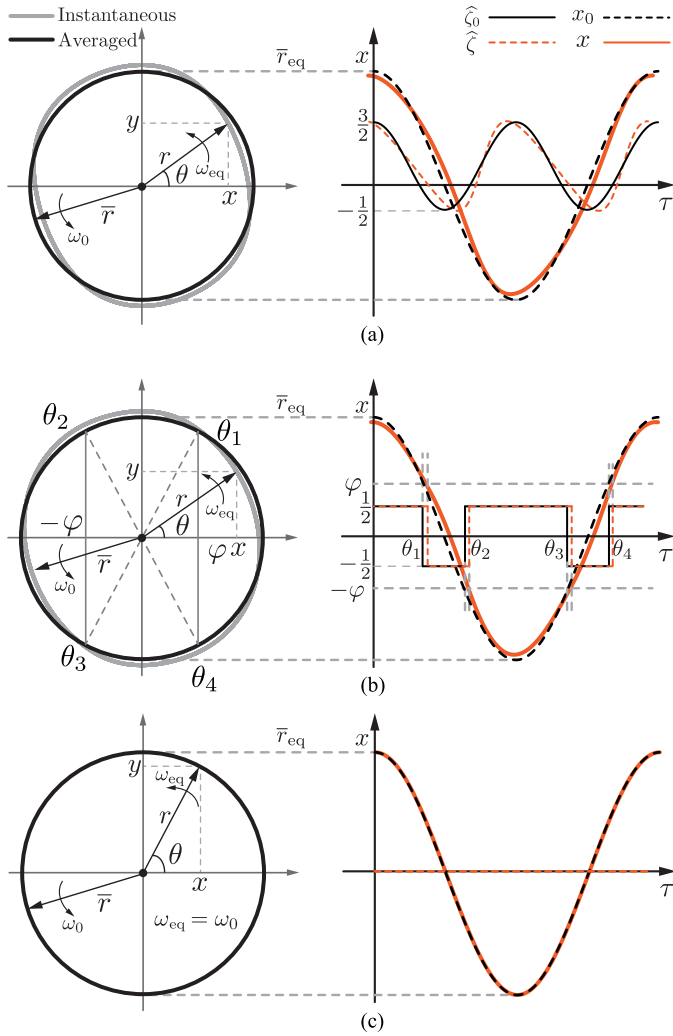


Fig. 4. Illustrating functions $\hat{\zeta}(\tau)$, $\hat{\zeta}_0(\tau)$ and trajectories $x(\tau)$, $x_0(\tau)$ for the: (a) Van der Pol, (b) dead-zone, (c) Andronov-Hopf oscillators.

While we are not interested in the solution to (54), we can infer the value of ω_2 to eliminate all secular terms in the solution. (In the case of ω_1 , the choice was immediately obvious; in this case, we will have to go through the dynamic models to establish the choice for each oscillator. We do so in sections that follow.) Once ω_2 is computed, the equilibrium frequency is estimated as

$$\omega_{eq} \approx \omega_0 + \epsilon^2 \omega_2. \quad (55)$$

C. Harmonic Properties of Oscillators

We now apply the general developments mentioned above to compute the third-to-fundamental harmonic ratio γ_3 and equilibrium frequency ω_{eq} for the three oscillators (see Fig. 4 for illustrations of key concepts and signals).

1) *Van Der Pol Oscillator*: Substituting $x_0 = \chi \cos \tau$ and the damping function from (11) in (51) yields

$$\hat{\zeta}_0 = \frac{1}{2} \left(\frac{3\alpha}{\sigma} \chi^2 \cos^2 \tau - 1 \right) \quad (56)$$

and (53) boils down to

$$x_1'' + x_1 = \left(\frac{3\alpha}{4\sigma} \chi^2 - 1 \right) \chi \sin \tau + \frac{3\alpha}{4\sigma} \chi^3 \sin 3\tau. \quad (57)$$

Notice that the driving terms mentioned above include $\sin \tau$ and $\sin 3\tau$ components. To suppress the secular term proportional to $\sin \tau$, we have to pick $\chi = 2\sqrt{\sigma/(3\alpha)}$. Notably, this amplitude is equal to the equilibrium amplitude \bar{r}_{eq} obtained via averaging, as discussed in Section III. With this value of χ , the solution for (57) is $x_1 = -1/4\sqrt{\sigma/(3\alpha)} \sin 3\tau$. It follows from (51) that $\hat{\zeta}_1 = -1/2 \sin 3\tau \cos \tau$, which when substituted in (54) gives

$$x_2'' + x_2 = \bar{r}_{eq} \left(\left(\frac{2\omega_2}{\omega_0} + \frac{1}{8} \right) \cos \tau + \frac{3}{8} \cos 3\tau + \frac{5}{8} \cos 5\tau \right).$$

To prevent secular terms, we have to pick $\omega_2 = -1/16\omega_0$, which when substituted into (55) yields the equilibrium frequency estimate in (31). This line of analysis yields results that mirror the ones in [39].

2) *Dead-Zone Oscillator*: Beginning once again with $x_0 = \chi \cos \tau$ and the damping function for the dead-zone oscillator in (12), it follows that $\hat{\zeta}_0 = 1/2$ when $x_0 > \varphi$, and $\hat{\zeta}_0 = -1/2$ when $x_0 < \varphi$. This can be expressed as the Fourier series

$$\hat{\zeta}_0 = a_0 + \sum_{n=1}^{\infty} a_{2n} \cos 2n\tau \quad (58)$$

with even-order coefficients given by

$$a_0 = \frac{2}{\pi} \phi - \frac{1}{2}, \quad a_{2n} = \frac{2}{n\pi} \sin 2n\phi \quad (59)$$

where $\phi = \cos^{-1}(\varphi/\chi)$ (odd-order terms are zero since the function is even). With these preliminaries in place, (53) yields

$$x_1'' + x_1 = (2a_0 - a_2)\chi \sin \tau + \sum_{n=1}^{\infty} (a_{2n} - a_{2(n+1)})\chi \sin((2n+1)\tau). \quad (60)$$

To eliminate secular terms, we need $2a_0 - a_2 = 0$. From (59) and $\phi = \cos^{-1}(\varphi/\chi)$, we get the algebraic constraint

$$\frac{4}{\pi} \cos^{-1} \left(\frac{\varphi}{\chi} \right) - 1 - \frac{4}{\pi} \varphi \frac{\sqrt{\chi^2 - \varphi^2}}{\chi^2} = 0. \quad (61)$$

This is identical to the algebraic constraint that yielded the steady-state averaged amplitude \bar{r}_{eq} in (24). The resulting solution for (60) is

$$x_1 = - \sum_{n=1}^{\infty} \frac{\bar{r}_{eq}}{4n^2 + 4n} (a_{2n} - a_{2(n+1)}) \sin((2n+1)\tau) \quad (62)$$

from which the value of γ_3 in (30) follows. The analysis mentioned above reveals that the third-to-fundamental harmonic content for the Van der Pol and dead-zone oscillators [see (29) and (30)] is proportional to $\epsilon\sigma$. Accordingly, a small value for $\epsilon\sigma$ results in a close to ideal sinusoidal waveform. Note from Remark 2 that this is in direct contrast to dynamic performance, highlighting a key design tradeoff.

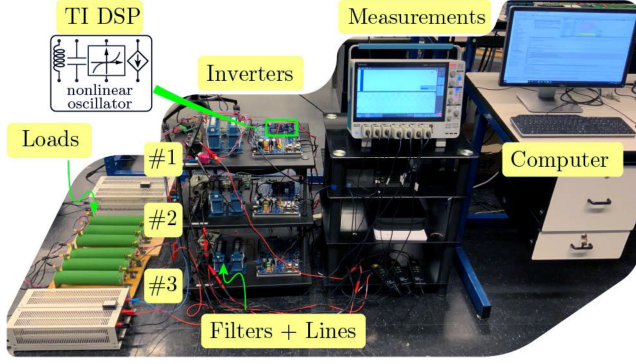


Fig. 5. Laboratory setup to validate performance of the nonlinear-oscillator controlled inverters.

Next, we obtain $\hat{\zeta}_1$ leveraging (54). To this end, we first note from (51) that

$$\hat{\zeta}_1 = x_1 \frac{\partial \hat{\zeta}_0}{\partial x} = x_1 \frac{\partial \hat{\zeta}_0}{\partial \tau} \frac{\partial \tau}{\partial x} = -\frac{\partial \hat{\zeta}_0}{\partial \tau} \frac{1}{\bar{r}_{\text{eq}} \sin \tau}.$$

The term $\partial \hat{\zeta}_0 / \partial \tau$ can be evaluated from (58). We then obtain

$$\hat{\zeta}_1 = \frac{2x_1}{r_{\text{eq}} \sin \tau} \sum_{n=1}^{\infty} n a_{2n} \sin 2n\tau. \quad (63)$$

Substituting $\hat{\zeta}_1$ from the abovementioned equation in (54) yields

$$x_2'' + x_2 = \left(\frac{2\omega_2}{\omega_0} + \sum_{n=1}^{\infty} \frac{(a_{2n} - a_{2(n+1)})^2}{4n^2 + 4n} \right) \bar{r}_{\text{eq}} \cos \tau + c_3 \bar{r}_{\text{eq}} \cos 3\tau + c_5 \bar{r}_{\text{eq}} \cos 5\tau. \quad (64)$$

Expressions for c_3 and c_5 are omitted since they are unnecessary in the forthcoming analysis. Secular terms attributed to the $\cos \tau$ term are suppressed with the choice

$$\omega_2 = -\frac{\omega_0}{2} \sum_{n=1}^{\infty} \frac{(a_{2n} - a_{2(n+1)})^2}{4n^2 + 4n}. \quad (65)$$

The expression for ω_{eq} in (32) results after substituting (65) into (32) and retaining the first four terms in the Fourier series (retaining additional terms has minimal impact on the numerical value). We observe that the steady-state frequency deviation from nominal $\omega_{\text{eq}} - \omega_0$ is proportional to $(\varepsilon\sigma)^2$ for the Van der Pol and dead-zone oscillators.

3) *Andronov-Hopf Oscillator*: From the generalized damping function for the Andronov-Hopf oscillator reported in (13), and the definition in (49), we get

$$\hat{\zeta}(x, y) = \frac{1}{2} \left(\frac{\alpha}{\sigma} (x^2 + y^2) - 1 \right). \quad (66)$$

Substituting $x_0 = \chi \cos \tau$ and $y_0 = \chi \sin \tau$ yields⁵

$$\hat{\zeta}(x_0, y_0) = \hat{\zeta}_0 = \frac{1}{2} \left(\frac{\alpha}{\sigma} \chi^2 - 1 \right). \quad (67)$$

⁵For $x_0 = \chi \cos \tau$, it follows that $y_0 = \chi \sin \tau$ from equating $\mathcal{O}(\varepsilon^0)$ terms in the series expansion of $y(\tau) = \omega_0 \omega_{\text{eq}}^{-1} \int x(\tau) d\tau$.

Then, (53) assumes the form

$$x_1'' + x_1 = \left(\frac{\alpha}{\sigma} \chi^2 - 1 \right) \chi \sin \tau. \quad (68)$$

The value $\chi = \sqrt{\alpha/\sigma}$ suppresses secular terms, and note that this is identical to the equilibrium of the averaged amplitude dynamics reported in (25). It follows that x_1 and y_1 are both zero, and (51) then suggests $\hat{\zeta}_1 = 0$. The $\mathcal{O}(\varepsilon^2)$ dynamics in (54) are

$$x_2'' + x_2 = -\frac{2\omega_2}{\omega_0} x_0''. \quad (69)$$

Secular terms are eliminated for $\omega_2 = 0$. These findings reveal that $\gamma_3 = 0$ and $\omega_{\text{eq}} = \omega_0$ for the Andronov-Hopf oscillator. In fact, following the same line of reasoning we see that higher-order terms in the expansion (48) are governed by

$$x_n'' + x_n = -\frac{2\omega_n}{\omega_0} x_0'', \quad n = 1, 2, \dots \quad (70)$$

Secular terms in all higher-order expressions are eliminated with the choice $\omega_n = x_n = 0 \forall n \neq 0$. The steady-state frequency is shown in (33), from which we know that the Andronov-Hopf oscillator generates harmonics-free oscillations with fundamental oscillation frequency equal to ω_0 .

V. DYNAMIC MODELING AND CONTROL DESIGN OF GFM INVERTERS WITH CURRENT FEEDBACK

In this section, we supplement the generalized mathematical analysis from prior sections to include current feedback and control scalings necessary for practical implementation. First, we establish dynamical models of the inverter terminal voltage and its frequency. Next, we provide a sketch of how the control parameters are selected to satisfy the performance criteria. Accordingly, this section lays the groundwork for controller implementation of all three oscillators.

A. Terminal-Voltage and Frequency Dynamics

Consider the single-phase hardware implementation in Fig. 1 with dc input voltage v_{dc} , a power stage, and an output filter. As illustrated in Fig. 1, the oscillator models in (5) and (7) have the current signal i_{in} extracted from them; this yields the dynamics

$$\begin{aligned} \dot{r} = & \varepsilon \omega_0 (\sigma r \cos \theta - f(r \cos \theta, r \sin \theta)) \cos \theta \\ & - \frac{\kappa_i i_{\text{in}}}{C} \cos \theta \end{aligned} \quad (71a)$$

$$\begin{aligned} \dot{\theta} = & \omega_0 - \varepsilon \omega_0 \left(\sigma \cos \theta - \frac{f(r \cos \theta, r \sin \theta)}{r} \right) \sin \theta \\ & - \frac{\kappa_i i_{\text{in}}}{C} \sin \theta. \end{aligned} \quad (71b)$$

With the transformation specified in (6), we can work out the following expressions for the control voltage signal v , and its orthogonal counterpart v_{\perp}

$$\begin{bmatrix} v \\ v_{\perp} \end{bmatrix} = \kappa_v \underbrace{\begin{bmatrix} \cos \phi & -\sin \phi \\ \sin \phi & \cos \phi \end{bmatrix}}_{=: R(\phi)} \begin{bmatrix} r \cos \theta \\ r \sin \theta \end{bmatrix} \quad (72)$$

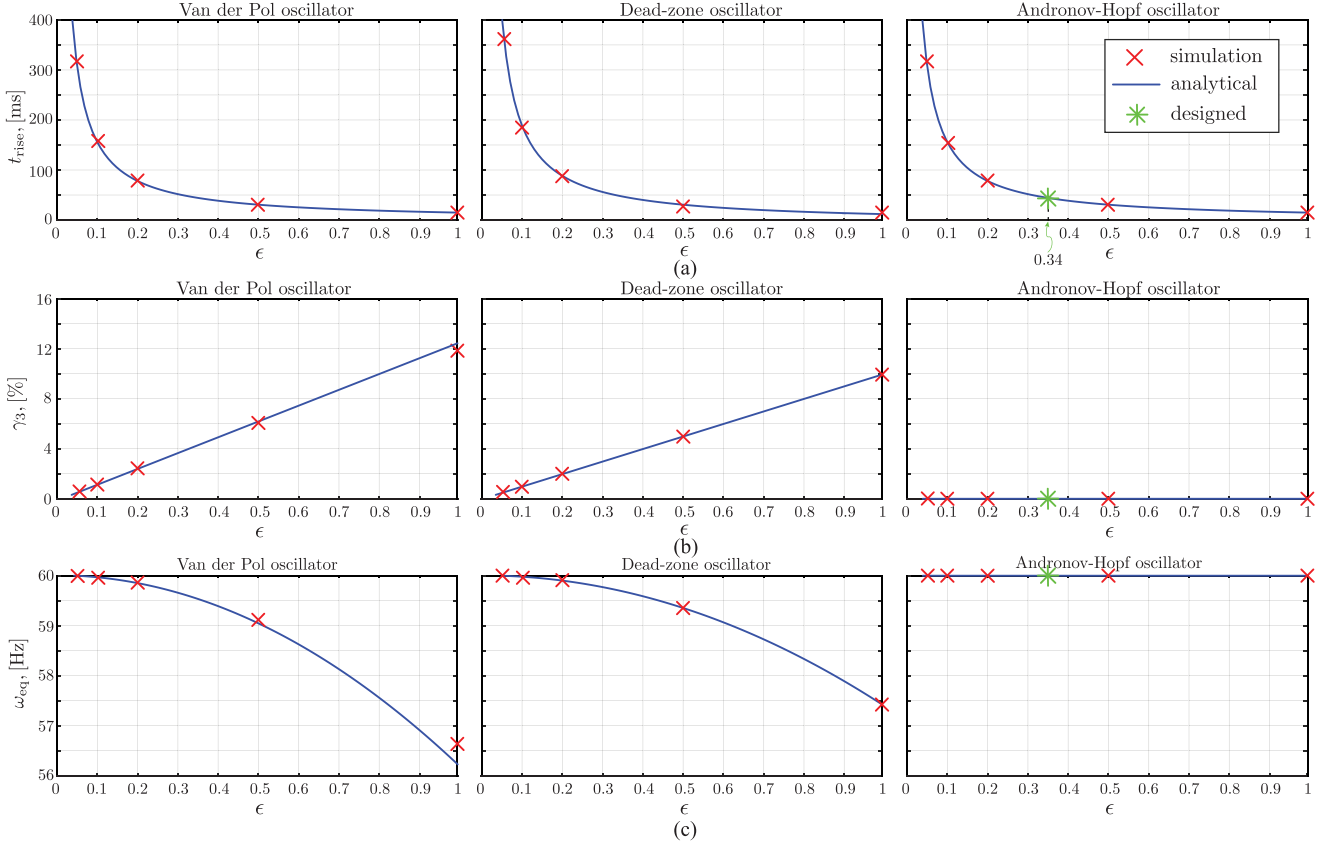


Fig. 6. Validation of analytical results via comparison with simulations for: (a) rise time t_{rise} , (b) harmonics γ_3 , and (c) steady-state frequency ω_{eq} . The operating point marked in green is indicative of what was implemented in the experiments in Section VI-C.

where $R(\phi)$ is a rotation matrix; ϕ is a user-defined angle that determines the relationship between voltage amplitude, frequency, real, and reactive power; and κ_v is a voltage scaling factor. The modulation signal is determined as $m = v/v_{\text{dc}}$. The switch-cycle-averaged terminal voltage, denoted as \tilde{v} in Fig. 1, tracks v . We subsequently refer to voltage v as the inverter terminal voltage. Since $R(\phi)$ only alter the angle but not amplitude, the RMS inverter voltage amplitude is

$$V = \frac{\kappa_v r}{\sqrt{2}} \quad (73)$$

and it follows $\dot{V} = \kappa_v \dot{r}/\sqrt{2}$. The oscillator input current is

$$i_{\text{in}} = \kappa_i (i_f - i_f^*) \quad (74)$$

where i_f is the measured current delivered by the switch terminals (see Fig. 1). The signal i_f^* is a reference signal that biases inverter operation and is derived from the active and reactive power setpoints P^* and Q^* , respectively. In particular, we express P^* and Q^* as follows:

$$P^* = 0.5(v i_f^* + v_{\perp} i_{\perp}^*), \quad Q^* = 0.5(v_{\perp} i_f^* - v i_{\perp}^*)$$

where i_{\perp}^* is the orthogonal signal of i_f^* . From the abovementioned discussion, we can isolate

$$i_f^* = 2 \frac{v P^* + v_{\perp} Q^*}{v^2 + v_{\perp}^2}. \quad (75)$$

TABLE III
PARAMETERS FOR PERFORMANCE EVALUATION

Type	Symbol	$\epsilon = \epsilon\sigma = 1/20$	$\epsilon = \epsilon\sigma = 1$	Units
VDP	ϵ	1/60	1/3	-
	σ	3	3	Ω^{-1}
	α	2	2	A/V^3
DZO	ϵ	1/60	1/3	-
	σ	3	3	Ω^{-1}
	φ	0.57	0.57	V
AHO	ϵ	1/60	1/3	-
	σ	3	3	Ω^{-1}
	α	1.5	1.5	A/V^3

We denote \bar{V} and $\bar{\theta}$ as the ac-cycle average of V and θ . Application of averaging theory yields the following dynamics for the averaged RMS voltage and phase

$$\dot{\bar{V}} = h(\bar{V}) - \frac{\kappa_v \kappa_i}{2C\bar{V}} ((P - P^*) \cos \phi + (Q - Q^*) \sin \phi) \quad (76a)$$

$$\dot{\bar{\theta}} = \omega_0 - \frac{\kappa_v \kappa_i}{2C\bar{V}^2} ((P - P^*) \sin \phi - (Q - Q^*) \cos \phi) \quad (76b)$$

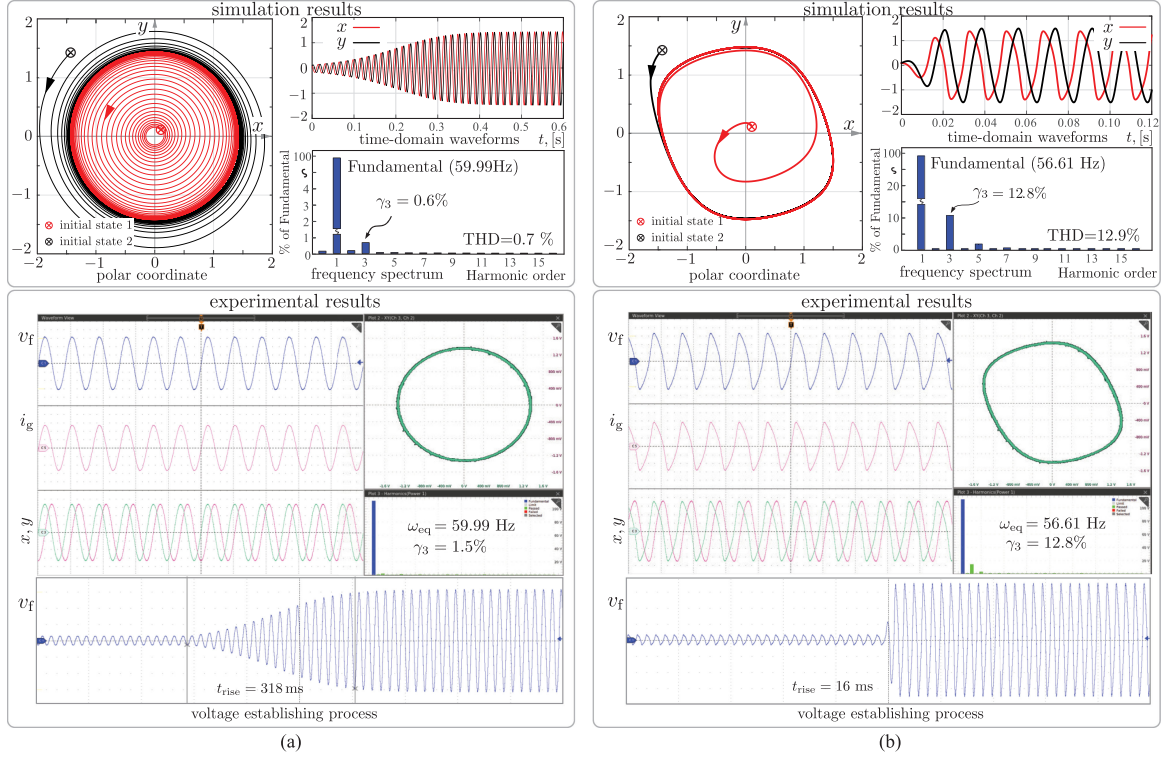


Fig. 7. Time-domain simulations and experimental results compared for the Van der Pol oscillator for: (a) $\epsilon = \epsilon\sigma = 1/20$ and (b) $\epsilon = \epsilon\sigma = 1$. Top panes: Simulations of trajectories illustrating convergence to periodic steady state (polar coordinates and time-domain waveforms; polar plots illustrate trajectories for two initial conditions) and frequency spectra. Middle panes: Corresponding experimental results. Bottom Panes: Terminal voltage startup in experiments.

where $h(\bar{V}) = \frac{\kappa_v}{\sqrt{2}} g(\frac{\sqrt{2}\bar{V}}{\kappa_v})$ represents the scaled version of averaged oscillator amplitude dynamics [see (37)] while the rest of the terms in (76a) result from the current feedback signal i_{in} . Meanwhile, (76b) gives the averaged phase dynamics with current feedback considered [also see (36)]. A short sketch of the derivation of the model in (76) is provided in Appendix E.

B. Design Methodology

The crux of the design procedure relies on computing the equilibria for (76) for a given rotation angle ϕ . Without the loss of generality, we focus on the case where $\phi = \frac{\pi}{2}$, which yields tradeoffs between $V - Q$ and $\omega - P$, respectively. This ϕ selection is best suited for inductive networks. Finally, we compute the equilibria of (76)—by setting $\dot{\bar{V}} = 0, \dot{\bar{\theta}} = 0$ —with real and reactive power setpoints P^* and Q^* set to zero. In this case, we obtain

$$0 = h(\bar{V}) - \frac{\kappa_v \kappa_i}{2C\bar{V}} S_{rated}, \quad \omega = \omega_0 - \frac{\kappa_v \kappa_i}{2C\bar{V}^2} S_{rated} \quad (77)$$

where $\omega = \dot{\bar{\theta}}$ denotes inverter frequency; S_{rated} is the rated apparent power. We evaluate voltage and frequency in (76) both at full load by setting $Q = S_{rated}$ and $P = S_{rated}$, respectively. We do so to certify the design for the worst-case condition. We further denote the nominal voltage rating as V_{nom} such that the voltage and current scalings are given by

$$\kappa_v = V_{nom}, \quad \kappa_i = \frac{V_{nom}}{S_{rated}}. \quad (78)$$

Under full load, the system will exhibit the largest deviations in steady-state voltage and frequency for all three oscillators. Given specifications on the maximum allowable voltage and frequency excursions along with rise-time and third harmonic metrics, this yields a system of algebraic equations for which the remaining parameters may be computed. In particular, the specified performance metrics yield an overdetermined system of algebraic equations where the values of $\alpha, \varphi, \sigma, L$, and C can be computed. A range of parameters that satisfy all performance requirements exist for most practical performance requirements. The interested reader can refer to [14] and [44] for established methods of designing the Van der Pol [49] and Andronov-Hopf oscillators, respectively, whereas the expressions in Table II can be applied for the dead-zone oscillator.

VI. NUMERICAL SIMULATIONS AND EXPERIMENTS

Numerical-model simulations and hardware experiments in this section focus on substantiating our prior analytical models. In particular, simulations are used to assess the validity of the derived performance metrics over a wide range of conditions for each oscillator, whereas experimental validations illustrate robust performance in practical implementations.

A. Implementation

To validate the analytical developments outlined thus far, we built a laboratory-scale experimental platform, as shown in Fig. 5. Inverter hardware corresponds to the configuration

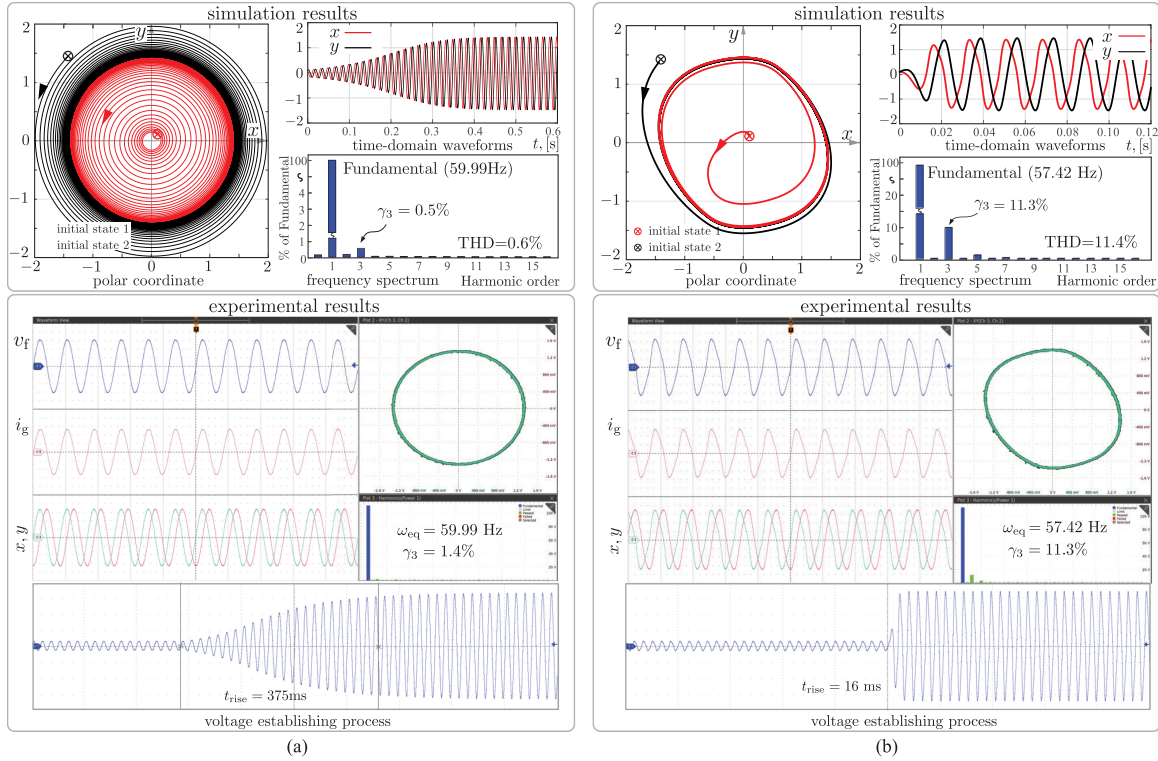


Fig. 8. Time-domain simulations and experimental results compared for the dead-zone oscillator for: (a) $\epsilon = \epsilon\sigma = 1/20$ and (b) $\epsilon = \epsilon\sigma = 1$. Top panes: Simulations of trajectories illustrating convergence to periodic steady state (polar coordinates and time-domain waveforms; polar plots illustrate trajectories for two initial conditions) and frequency spectra. Middle panes: Corresponding experimental results. Bottom Panes: Terminal voltage startup in experiments.

in Fig. 1. An H-bridge inverter unit delivers power to the ac side through an *LCL* filter with inverter-side inductance L_1 , capacitance C_f , and load-side inductance L_2 . Both switching and sampling frequencies are set as $f_{sw} = f_{sam} = 10$ kHz. Texas Instruments TMS320F28379D digital signal processors execute the discretized nonlinear oscillator dynamics. The controller dynamics from (1) with current feedback are discretized with Tustin's method using a time step equal to the switching period $T_{sw} = 10^{-4}$ s.

B. Performance Evaluation

The first experiments are designed to verify the output characteristics of three nonlinear oscillators without current feedback. Parameters to realize the oscillator dynamics are adopted from Table III. The rise time t_{rise} , third-to-fundamental harmonics γ_3 , and equilibrium frequency ω_{eq} are three main indices we focus on. In each experiment, we determine the σ/α ratio and φ value to guarantee oscillator amplitude $\bar{r}_{eq} = \sqrt{2}$ [see (23)–(25)]. The values of L and C are tuned to obtain different values of ϵ while ensuring the frequency $\omega_0 = 1/\sqrt{LC} = 2\pi 60$ rad/s. Fig. 6 illustrates analytically calculated and numerically evaluated values of rise time t_{rise} , third-to-fundamental harmonics γ_3 , and steady-state frequency ω_{eq} for the Van der Pol, dead-zone, and Andronov-Hopf oscillators. Numerical simulations are performed for $\epsilon = \epsilon\sigma = 1/20, 1/10, 1/5, 1/2, 1$ and are able to capture full-order nonlinear dynamics with high fidelity. The simulations closely match the analytically computed results

(refer to Table II) across the full range of $\epsilon\sigma$ values considered, thus substantiating our proposed models. Reflecting on the waveforms for all three oscillators in Fig. 6(a), it is clear that rise time is inversely proportional to ϵ , while Fig. 6(b) shows that harmonic content is directly proportional to ϵ . It is also clear that the Van der Pol and dead-zone oscillators exhibit a tradeoff between rise time and harmonics (as was also established in the analytical derivations). In contrast, such a tradeoff is absent for the Andronov-Hopf oscillator.

Figs. 7–9 illustrate analytically computed and experimentally generated trajectories and frequency spectra for the three oscillators under disparate values of ϵ . Capacitor voltage v_f and grid-side current i_g are plotted in the figures. Results are shown in Table IV. Overall, we observe a close match between analytical calculations and experiments. Modest mismatches between simulation and experiment appear for γ_3 when ϵ is small. This is because the distortion originating from the oscillator itself is sufficiently small that nonidealities from PWM switching dominate the hardware measurement of γ_3 .

C. Inverter-Based System With GFM Control

To highlight a practical use case, we next consider an experiment consisting of three inverters programmed with Andronov-Hopf oscillators, two loads, and a three-bus network with line impedances, shown in Fig. 10. The dc voltage sources are implemented with regenerative power supplies that enable the inverters to source and sink power. The controllers are designed to

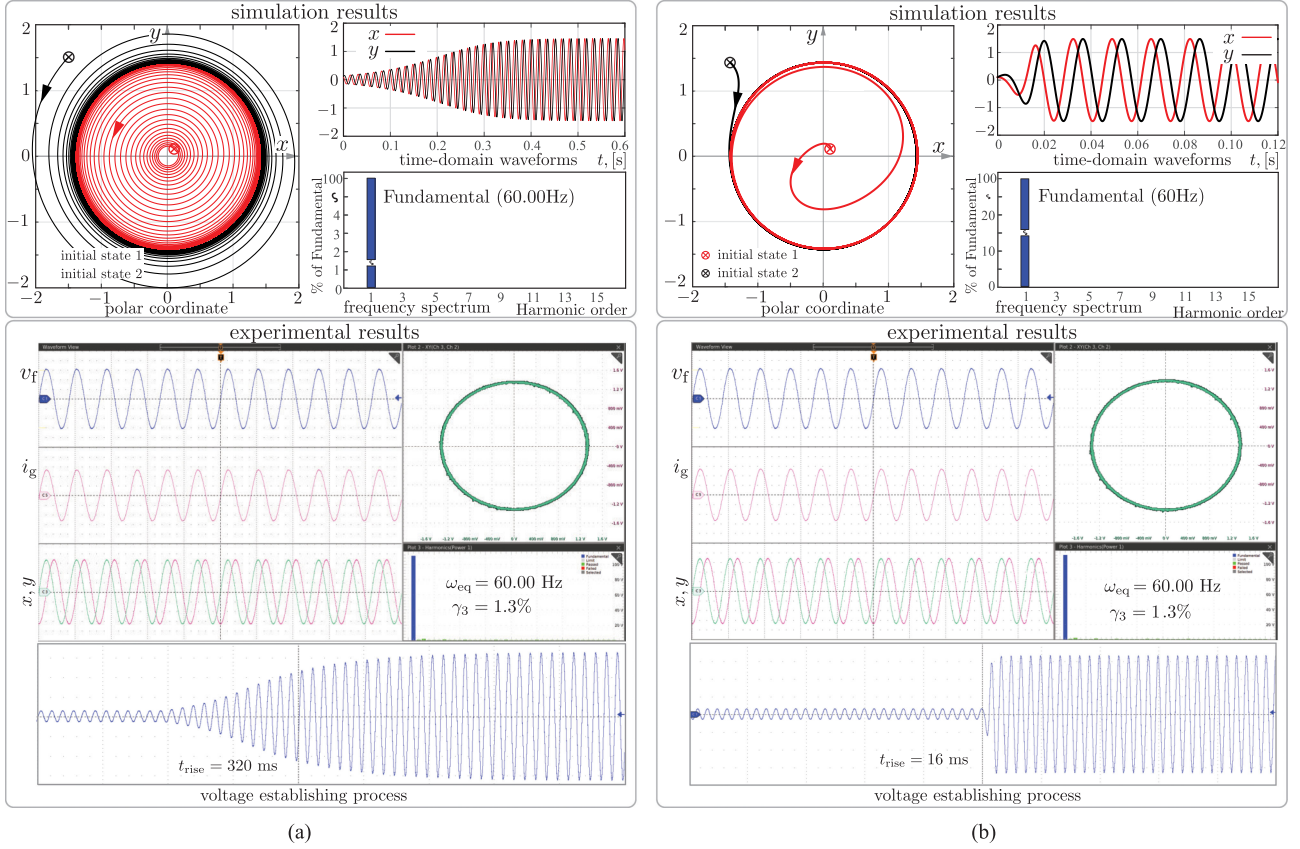


Fig. 9. Time-domain simulations and experimental results compared for the Andronov-Hopf oscillator for: (a) $\epsilon = \epsilon\sigma = 1/20$ and (b) $\epsilon = \epsilon\sigma = 1$. Top panes: Simulations of trajectories illustrating convergence to periodic steady state (polar coordinates and time-domain waveforms; polar plots illustrate trajectories for two initial conditions) and frequency spectra. Middle panes: Corresponding experimental results. Bottom Panes: Terminal voltage startup in experiments.

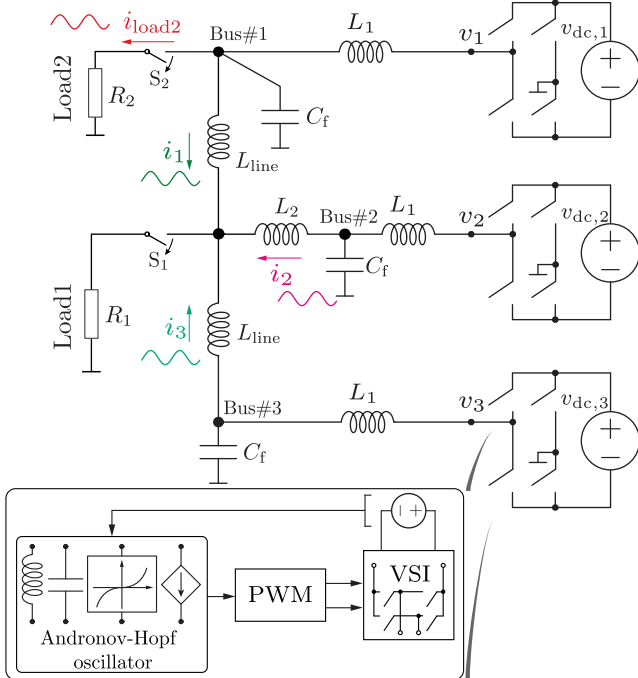


Fig. 10. GFM application with Andronov-Hopf oscillator controller.

ensure a nominal $80 \text{ V}_{\text{rms}}$ voltage at 60 Hz , 5% voltage deviation across the full load range, no more than 2% of third-harmonic content, and less than 50 ms rise-time. Substituting (78) in (77), substituting $h(\bar{V}) = \frac{\kappa_v}{\sqrt{2}} g(\frac{\sqrt{2}\bar{V}}{\kappa_v})$ with $g(\cdot)$ given in (22), and solving for the roots of voltage equilibria from the algebraic equation that results, we can write the equilibrium voltage and frequency deviation as

$$\bar{V}_{\text{eq}} = \frac{V_{\text{nom}}}{\sqrt{2}} \sqrt{1 + \sqrt{1 - \frac{4}{\sigma}}}, \quad \Delta\omega = \frac{V_{\text{nom}}^2}{V_{\text{eq}}^2} \frac{1}{2C} \quad (79)$$

where $V_{\text{nom}} = \kappa_v \sqrt{\sigma/2\alpha}$. From (25), we select $\sigma/\alpha = 2$ to achieve an oscillator RMS amplitude of one.

From (79), it follows that

$$\sigma = \frac{V_{\text{nom}}^4}{V_{\text{min}}^2 (V_{\text{nom}}^2 - V_{\text{min}}^2)}, \quad \varepsilon \leq 2 \frac{|\Delta\omega|_{\text{max}}}{\omega_0} \frac{V_{\text{min}}^2}{V_{\text{nom}}^2}$$

where $C = 1/(\varepsilon\omega_0)$. Moreover, the rise time boundary

$$t_{\text{rise}} = \frac{6}{\varepsilon\sigma\omega_0} \leq t_{\text{rise,max}}$$

leads to an additional constraint $\varepsilon\sigma \geq 6/(t_{\text{rise,max}}\omega_0)$. Parameters that satisfy these constraints are in Table V. The selected $\epsilon = \epsilon\sigma$ for the experiments is marked in green in Fig. 6.

TABLE IV
MEASURED AND SIMULATED PERFORMANCE METRICS

Symbol		$\epsilon = \epsilon\sigma = 1/20$			$\epsilon = \epsilon\sigma = 1$		
		Cal.	Sim.	Exp.	Cal.	Sim.	Exp.
Van der Pol	\bar{r}_{eq} [V]	$\sqrt{2}$	1.414	1.410	$\sqrt{2}$	1.414	1.410
	t_{rise} [ms]	318	321	320	15.9	16.7	17.0
	γ_3 [%]	0.50	0.60	1.50	12.5	11.8	12.8
	ω_{eq} [Hz]	59.99	59.99	59.99	56.25	56.60	56.61
Dead-zone	\bar{r}_{eq} [V]	$\sqrt{2}$	1.414	1.414	$\sqrt{2}$	1.414	1.414
	t_{rise} [ms]	363	359	365	18.1	17.0	17.0
	γ_3 [%]	0.5	0.5	1.4	9.9	10.0	11.3
	ω_{eq} [Hz]	59.99	59.99	59.99	57.40	57.41	57.42
Andronov-Hopf	\bar{r}_{eq} [V]	$\sqrt{2}$	1.414	1.414	$\sqrt{2}$	1.414	1.414
	t_{rise} [ms]	318	319	320	15.9	16.0	16.0
	γ_3 [%]	0	0	1.30	0	0	1.30
	ω_{eq} [Hz]	60.00	60.00	60.00	60.00	60.00	60.00

TABLE V
SYSTEM PARAMETERS WITH CURRENT FEEDBACK

	Symbol	Description	Value	Units
Inverter	S_{rated}	Power rating	320	W
	V_{nom}	Nominal RMS voltage	80	V
	V_{min}	Minimum voltage	0.95×80	V
	ω_0	Nominal frequency	$2\pi \times 60$	rad/s
	$ \Delta\omega _{max}$	Maximum frequency offset	$2\pi \times 0.5$	rad/s
	$\gamma_{3,max}$	Maximum third harmonics	2%	-
	$t_{rise,max}$	Maximum rise time	50	ms
	L_1	LCL -filter Inductance	1.5	mH
	C_f	LCL -filter Capacitance	10	μF
	L_2	LCL -filter Inductance	1.5	mH
Network	L_{line}	Inductance	1.5	mH
	P_{load1}	Load power 1	220	W
	P_{load2}	Load power 2	220	W
Oscillator	κ_v	Voltage scaling	80	V/V
	κ_i	Current scaling	0.25	A/A
	α	-	5.68	V
	σ	-	11.36	Ω^{-1}
	ϵ	-	0.03	-
	$\epsilon = \epsilon\sigma$	-	0.34	-
	C	Virtual capacitance	0.0884	F
	L	Virtual inductance	79.58	μH
	ϕ	Rotation angle	$\pi/2$	rad

Each inverter also has a distinct set of real power commands, denoted as P_1 , P_2 , and P_3 that we modulate to illustrate adjustable power sharing among the three inverters. Fig. 10 illustrates the experimental setup. We begin with no loads connected to the system (i.e., S_1 and S_2 are open). Initially, P_1 is set to a negative value while both P_2 and P_3 are fixed at zero. Given the absence of load power, inverters #2 and #3 deliver power which is then absorbed by inverter #1. Subsequently, P_1 is

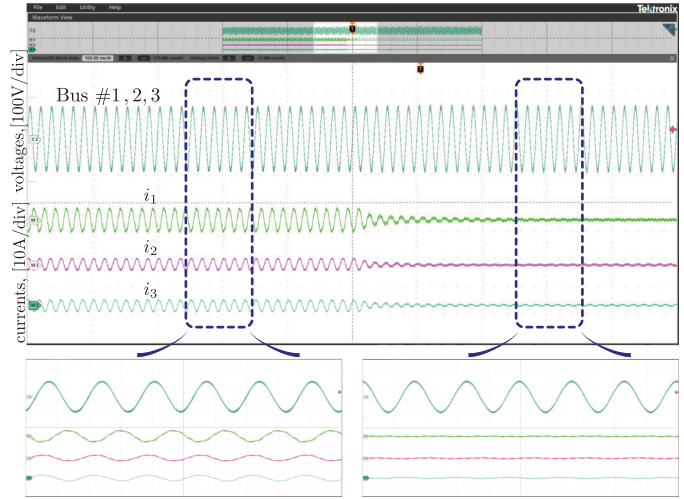


Fig. 11. Interconnected without load, S_1 and S_2 are open: i) $P_1^* = -200W$, #2 and #3 inverters deliver power to #1 inverter and ii) $P_1^* = 0W$.

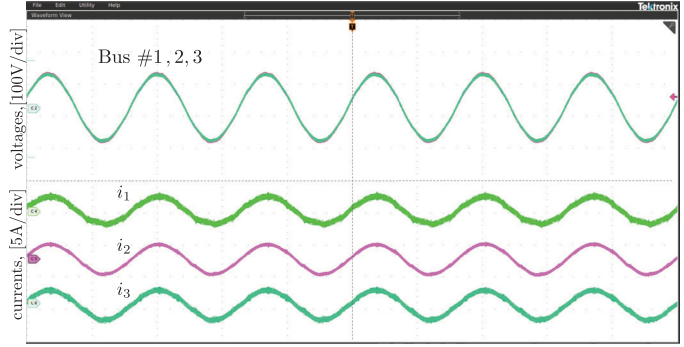


Fig. 12. Supplying Load1 only: S_1 closed and S_2 open.

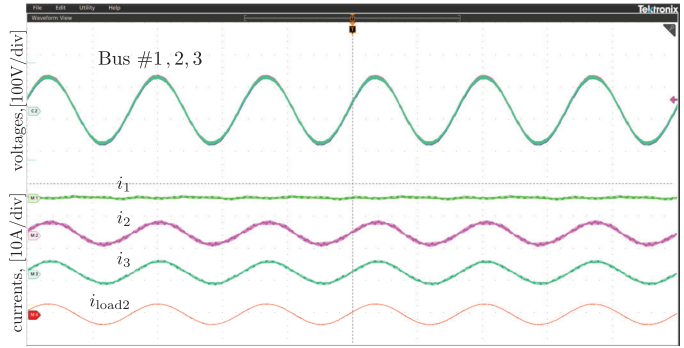


Fig. 13. Supplying Load1 and Load2: S_1 and S_2 closed and $P_{load2} = \frac{1}{2} P_{load1}$.

brought back to zero and each inverter delivers zero current. This highlights how the control accommodates bidirectional power flow. Next, Figs. 12 and 13 show the measured waveforms when the inverters deliver power into one and then both loads, respectively, when P_1 , P_2 , and P_3 are all fixed at zero. Here, the uniform power setpoints give near-equal power sharing. Finally, Fig. 14 illustrates nonuniform power sharing after P_1 is adjusted once again to a negative value.

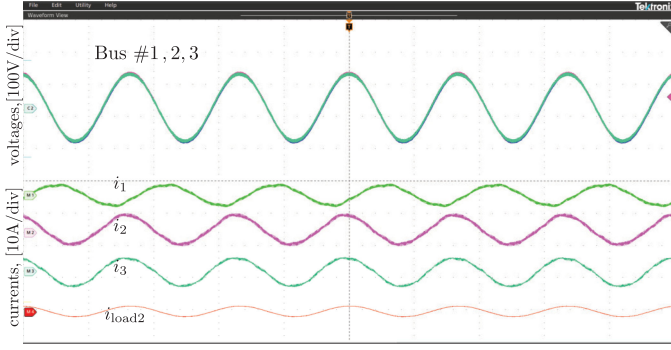


Fig. 14. Decrease load 2: $P_{\text{load}2} = \frac{1}{4} P_{\text{load}1}$ and $P_1^* = -200\text{W}$.

VII. CONCLUSION

This article established a generic modeling framework to characterize the properties of second-order nonlinear circuits composed of a harmonic oscillator and state-dependent damping. Averaging analysis uncovered amplitude dynamics and perturbation theory allowed us to characterize steady-state frequency and harmonics. These methods were applied to Van der Pol, dead-zone, and Andronov-Hopf oscillators, which exhibit a wide array of properties and served to illustrate the generality of our approach. Further analysis is used to characterize system dynamics in the presence of an output load and additional parametric scalings needed for implementation. These additional results inform a design process needed for practical hardware applications. After computing the key properties of these oscillators, their models were validated numerically and in a variety of experiments. Extending the complete analytical framework on harmonics, rise time, and small-signal stability to include loads and network interactions while acknowledging current feedback is an important direction for future work. Furthermore, extending the stability analysis to large-signal methods, and perturbation analysis to higher-order terms would provide more accurate and comprehensive insights on dynamic and harmonic properties.

APPENDIX

A. Derivation of (3) and (4)

Rewriting (1) in second-order form yields

$$\ddot{x} + \varepsilon \omega_0 \left(\dot{f}(x, y) - \sigma \dot{x} \right) + \omega_0^2 x = 0. \quad (80)$$

We expand the derivative $\dot{f}(x, y)$ as follows:

$$\begin{aligned} \dot{f}(x, y) &= \frac{\partial f}{\partial x} \dot{x} + \frac{\partial f}{\partial y} \dot{y} \\ &= \frac{\partial f}{\partial x} \dot{x} + \frac{\partial f}{\partial y} \omega_0 x = \frac{\partial f}{\partial x} \dot{x} + \frac{\partial f}{\partial y} \frac{x}{y} \omega_0 y \\ &= \frac{\partial f}{\partial x} \dot{x} + \frac{\partial f}{\partial y} \frac{x}{y} (\varepsilon \omega_0 (\sigma x - f(x, y)) - \dot{x}) \\ &= \left(\frac{\partial f}{\partial x} - \frac{\partial f}{\partial y} \frac{x}{y} \right) \dot{x} + \frac{\partial f}{\partial y} \frac{\varepsilon \omega_0 (\sigma x - f(x, y))}{y} x. \end{aligned}$$

Substituting $\dot{f}(x, y)$ to (80) yields

$$\begin{aligned} \ddot{x} + 2 \underbrace{\frac{\varepsilon}{2} \left(\frac{\partial f}{\partial x} - \frac{\partial f}{\partial y} \frac{x}{y} - \sigma \right)}_{=\zeta(x, y)} \omega_0 \dot{x} \\ + \underbrace{\omega_0^2 \left(1 + \varepsilon^2 \frac{\sigma x - f(x, y)}{y} \frac{\partial f}{\partial y} \right)}_{=\omega^2(x, y)} x = 0 \end{aligned}$$

which matches (2) with $\zeta(x, y)$ and $\omega(x, y)$ listed in (3) and (4), respectively.

B. Derivation of (1) from (5)

From Fig. 1, we give the LC resonant circuit dynamics as [also see (5)]

$$\begin{aligned} C \dot{v}_C &= -i_L - f(v_C, i_L) + \sigma v_C \\ L \dot{i}_L &= v_C \end{aligned}$$

where v_C and i_L are circuit states. Recalling the definitions as follows:

$$\varepsilon := \sqrt{\frac{L}{C}}, \quad \omega_0 := \sqrt{\frac{1}{LC}}$$

we know $C = 1/(\varepsilon \omega_0)$ and $L = \varepsilon/\omega_0$. Substituting C and L expressions to circuit dynamics mentioned above yields

$$\begin{aligned} \dot{v}_C &= -\varepsilon \omega_0 i_L - \varepsilon \omega_0 f(v_C, i_L) + \varepsilon \omega_0 \sigma v_C \\ \varepsilon \dot{i}_L &= \omega_0 v_C. \end{aligned}$$

We select system states as $x = v_C$ and $y = \varepsilon i_L$, and obtain the following standard dynamics in (1) as

$$\begin{aligned} \dot{x} &= \varepsilon \omega_0 (\sigma x - f(x, y)) - \omega_0 y \\ \dot{y} &= \omega_0 x. \end{aligned}$$

C. Dead-Zone Oscillator Averaged Amplitude Dynamics

For $\bar{r} < \varphi$, we have from (15) that

$$\dot{\bar{r}} = \int_{\theta=0}^{2\pi} \varepsilon \omega_0 \sigma \bar{r} \cos^2 \theta d\theta = \frac{\varepsilon \omega_0 \sigma}{2} \bar{r}. \quad (81)$$

For $\bar{r} \geq \varphi$, the averaged amplitude dynamics are given by

$$\dot{\bar{r}} = \frac{1}{2\pi} \left(\int_{\theta_1}^{\theta_2} \dot{\bar{r}} d\theta + \int_{\theta_2}^{\theta_3} \dot{\bar{r}} d\theta + \int_{\theta_3}^{\theta_4} \dot{\bar{r}} d\theta + \int_{\theta_4}^{\theta_1} \dot{\bar{r}} d\theta \right) \quad (82)$$

where $\theta_1, \dots, \theta_4$ take the form in (34). The integrands follow from (15). Trigonometric and algebraic manipulations to simplify (82) combined with (81) yield the averaged amplitude dynamics reported in (21).

D. Dead-Zone Oscillator Rise Time

The calculation for the rise time has to be carried out by breaking up the pertinent integrals over intervals where averaged amplitude dynamics are continuous. From the definition for rise

time in (39), we have

$$\begin{aligned} t_{\text{rise}} &= \int_{0.1\bar{r}_{\text{eq}}}^{\varphi} \frac{2}{\varepsilon\sigma\omega_0} \frac{1}{\bar{r}} d\bar{r} \\ &+ \int_{\varphi}^{0.9\bar{r}_{\text{eq}}} \frac{\pi}{2\varepsilon\sigma\omega_0} \frac{1}{\left[\frac{\varphi}{\bar{r}}\sqrt{\bar{r}^2 - \varphi^2} + \left(\frac{\pi}{4} - \arccos\frac{\varphi}{\bar{r}}\right)\bar{r}\right]} d\bar{r} \\ &\approx \frac{6.84}{\varepsilon\sigma\omega_0}. \end{aligned}$$

E. Derivation of Polar Dynamics in (76)

Recalling voltages v and v_{\perp} in (72), we get

$$v = \kappa_v r \cos \psi, \quad v_{\perp} = \kappa_v r \sin \psi$$

where the phase angle of voltage v is $\psi = \theta + \phi$. Leveraging the relationship $V = \kappa_v r / \sqrt{2}$ in (73), we know

$$\bar{V} = \frac{1}{2\pi} \int_0^{2\pi} \frac{\kappa_v}{\sqrt{2}} r d\theta$$

and averaging the dynamics (71) over one ac cycle yields

$$\begin{aligned} \dot{\bar{V}} &= h(\bar{V}) - \frac{1}{2\pi} \int_{\theta=0}^{2\pi} \frac{\kappa_v i_{\text{in}}}{\sqrt{2}C} \cos \theta d\theta \\ \dot{\bar{\theta}} &= \omega_0 - \frac{1}{2\pi} \int_{\theta=0}^{2\pi} \frac{\kappa_v i_{\text{in}}}{\sqrt{2}C} \sin \theta d\theta \end{aligned}$$

where the function $h(\cdot)$ relates to (37), which represents the oscillator dynamics without current feedback. Consider the following series of steps for simplifying the integral term in the averaged-voltage dynamics

$$\begin{aligned} \frac{1}{2\pi} \int_{\theta=0}^{2\pi} i_{\text{in}} \cos \theta d\theta &= \frac{1}{2\pi} \int_{\theta=0}^{2\pi} \frac{1}{V} V i_{\text{in}} \cos \theta d\theta \\ &= \frac{1}{2\pi} \int_{\psi=\phi}^{2\pi+\phi} \frac{1}{V} V i_{\text{in}} \cos (\psi - \phi) d\psi \\ &= \frac{1}{2\pi} \int_{\psi=\phi}^{2\pi+\phi} \frac{1}{V} V i_{\text{in}} (\cos \psi \cos \phi + \sin \psi \sin \phi) d\psi \\ &= \frac{1}{2\pi} \int_{\psi=\phi}^{2\pi+\phi} \frac{1}{V} (v i_{\text{in}} \cos \phi + v_{\perp} i_{\text{in}} \sin \phi) d\psi \\ &= \frac{\kappa_i}{2\pi} \int_{\psi=\phi}^{2\pi+\phi} \frac{1}{V} (v (i_{\text{f}} - i_{\text{f}}^*) \cos \phi + v_{\perp} (i_{\text{f}} - i_{\text{f}}^*) \sin \phi) d\psi \\ &= \frac{\kappa_i}{V} ((P - P^*) \cos \phi + (Q - Q^*) \sin \phi). \end{aligned}$$

In the steps mentioned above, we have utilized (72)–(75), the following definitions for the instantaneous real and reactive power outputs of the inverter

$$P = \frac{1}{2\pi} \int_{\psi=\phi}^{2\pi+\phi} v i_{\text{f}} d\psi, \quad Q = \frac{1}{2\pi} \int_{\psi=\phi}^{2\pi+\phi} v_{\perp} i_{\text{f}} d\psi$$

and the fact that

$$\frac{1}{2\pi} \int_{\psi=\phi}^{2\pi+\phi} v i_{\text{f}}^* d\psi = \frac{1}{2\pi} \int_{\psi=\phi}^{2\pi+\phi} v \frac{v P^* + v_{\perp} Q^*}{V^2} d\psi$$

$$= \frac{1}{2\pi} \int_{\psi=\phi}^{2\pi+\phi} 2P^* \cos^2 \psi + 2Q^* \cos \psi \sin \psi d\psi = P^*$$

and

$$\begin{aligned} \frac{1}{2\pi} \int_{\psi=\phi}^{2\pi+\phi} v_{\perp} i_{\text{f}}^* d\psi &= \frac{1}{2\pi} \int_{\psi=\phi}^{2\pi+\phi} v_{\perp} \frac{v P^* + v_{\perp} Q^*}{V^2} d\psi \\ &= \frac{1}{2\pi} \int_{\psi=\phi}^{2\pi+\phi} 2P^* \cos \psi \sin \psi + 2Q^* \sin^2 \psi d\psi = Q^*. \end{aligned}$$

As mentioned above, we have leveraged the definition (75), and the identities $1/2\pi \int_0^{2\pi} \cos^2 \psi d\psi = 1/2\pi \int_0^{2\pi} \sin^2 \psi d\psi = 1/2$ and $\int_0^{2\pi} \cos \psi \sin \psi d\psi = 0$. The integral term in the averaged-phase dynamics simplifies similarly.

F. Derivation of (79)

Referring to (22), we obtain the $h(\bar{V})$ as

$$h(\bar{V}) = \frac{\kappa_v}{\sqrt{2}} g \left(\frac{\sqrt{2} \bar{V}}{\kappa_v} \right) = \frac{\sigma \bar{V}}{2C} \left(1 - \frac{\bar{V}^2}{V_{\text{nom}}^2} \right)$$

where $V_{\text{nom}} = \kappa_v \sqrt{\frac{\sigma}{2\alpha}}$. Then, (77) becomes

$$0 = \sigma \bar{V}^2 \left(1 - \frac{\bar{V}^2}{V_{\text{nom}}^2} \right) - \kappa_v \kappa_i S_{\text{rated}}.$$

Substituting κ_v and κ_i from (78) into the expression mentioned above yields

$$0 = \bar{V}^4 - V_{\text{nom}}^2 \bar{V}^2 + \frac{V_{\text{nom}}^4}{\sigma}.$$

Solving for V_{eq} gives (79).

REFERENCES

- [1] J. Rocabert, A. Luna, F. Blaabjerg, and P. Rodríguez, "Control of power converters in AC microgrids," *IEEE Trans. Power Electron.*, vol. 27, no. 11, pp. 4734–4749, Nov. 2012.
- [2] D. Pan, X. Wang, F. Liu, and R. Shi, "Transient stability of voltage-source converters with grid-forming control: A design-oriented study," *IEEE Trans. Emerg. Sel. Topics Power Electron.*, vol. 8, no. 2, pp. 1019–1033, Jun. 2020.
- [3] Y. Lin *et al.*, "Pathways to the next-generation power system with inverter-based resources: Challenges and recommendations," *IEEE Electrific. Mag.*, vol. 10, no. 1, pp. 10–21, Mar. 2022.
- [4] P. Unruh, M. Nuschke, P. Strauß, and F. Welck, "Overview on grid-forming inverter control methods," *Energies*, vol. 13, no. 10, 2020, Art. no. 2589.
- [5] H. Wu and X. Wang, "Design-oriented transient stability analysis of grid-connected converters with power synchronization control," *IEEE Trans. Ind. Electron.*, vol. 66, no. 8, pp. 6473–6482, Aug. 2019.
- [6] A. Tayyebi, A. Anta, and F. Dörfler, "Almost globally stable grid-forming hybrid angle control," in *Proc. 59th IEEE Conf. Decis. Control*, 2020, pp. 830–835.
- [7] L. A. Törres, J. P. Hespanha, and J. Moehlis, "Synchronization of identical oscillators coupled through a symmetric network with dynamics: A constructive approach with applications to parallel operation of inverters," *IEEE Trans. Autom. Control*, vol. 60, no. 12, pp. 3226–3241, Dec. 2015.
- [8] M. Sinha, F. Dörfler, B. Johnson, and S. Dhople, "Uncovering droop control laws embedded within the nonlinear dynamics of Van der Pol oscillators," *IEEE Trans. Control Netw. Syst.*, vol. 4, no. 2, pp. 347–358, Jun. 2017.
- [9] S. A. Aghdam and M. Agamy, "Virtual oscillator-based methods for grid-forming inverter control: A review," *IET Renew. Power Gener.*, vol. 16, pp. 835–855, 2022.

- [10] M. Colombino, D. Groz, J.-S. Brouillon, and F. Dörfler, "Global phase and magnitude synchronization of coupled oscillators with application to the control of grid-forming power inverters," *IEEE Trans. Autom. Control*, vol. 64, no. 11, pp. 4496–4511, Nov. 2019.
- [11] B. Johnson, S. Dhople, A. Hamadeh, and P. Krein, "Synchronization of parallel single-phase inverters with virtual oscillator control," *IEEE Trans. Power Electron.*, vol. 29, no. 11, pp. 6124–6138, Nov. 2014.
- [12] M. A. Awal and I. Husain, "Unified virtual oscillator control for grid-forming and grid-following converters," *IEEE Trans. Emerg. Sel. Topics Power Electron.*, vol. 9, no. 4, pp. 4573–4586, Aug. 2021.
- [13] H. Yu, M. A. Awal, H. Tu, I. Husain, and S. Lukic, "Comparative transient stability assessment of droop and dispatchable virtual oscillator controlled grid-connected inverters," *IEEE Trans. Power Electron.*, vol. 36, no. 2, pp. 2119–2130, Feb. 2021.
- [14] M. Lu, S. Dutta, V. Purba, S. Dhople, and B. Johnson, "A grid-compatible virtual oscillator controller: Analysis and design," in *Proc. IEEE Energy Convers. Congr. Expo.*, Sep. 2019, pp. 2643–2649.
- [15] M. Li, Y. Gui, Y. Guan, J. Matas, J. M. Guerrero, and J. C. Vasquez, "Inverter parallelization for an islanded microgrid using the Hopf oscillator controller approach with self-synchronization capabilities," *IEEE Trans. Ind. Electron.*, vol. 68, no. 11, pp. 10879–10889, Nov. 2021.
- [16] M. Lu, R. Mallik, B. Johnson, and S. Dhople, "Dispatchable virtual-oscillator-controlled inverters with current-limiting and MPPT capabilities," in *Proc. Energy Convers. Congr. Expo.*, 2021, pp. 3316–3323.
- [17] O. Ajala, M. Lu, S. Dhople, B. B. Johnson, and A. Dominguez-Garcia, "Model reduction for inverters with current limiting and dispatchable virtual oscillator control," *IEEE Trans. Energy Convers.*, early access, May 25, 2021, doi: [10.1109/TEC.2021.3083488](https://doi.org/10.1109/TEC.2021.3083488).
- [18] J. Li, M. Ali, J. E. Fletcher, and H. I. Nurdin, "Modeling and analysis of multiple inverters with dual-loop based virtual oscillator control," *IEEE Trans. Emerg. Sel. Topics Power Electron.*, early access, Nov. 18, 2021, doi: [10.1109/JESTPE.2021.3129083](https://doi.org/10.1109/JESTPE.2021.3129083).
- [19] B. Johnson, S. Dhople, A. Hamadeh, and P. Krein, "Synchronization of nonlinear oscillators in an LTI electrical power network," *IEEE Trans. Circuits Syst. I: Regular Papers*, vol. 61, no. 3, pp. 834–844, Mar. 2014.
- [20] J. Lynch and R. York, "Synchronization of oscillators coupled through narrow-band networks," *IEEE Trans. Microw. Theory Techn.*, vol. 49, no. 2, pp. 237–249, Feb. 2001.
- [21] P. Maffezzoni, "Synchronization analysis of two weakly coupled oscillators through a PPV macromodel," *IEEE Trans. Circuits Syst. I: Regular Papers*, vol. 57, no. 3, pp. 654–663, Jun. 2010.
- [22] S. Dhople, B. Johnson, F. Dörfler, and A. Hamadeh, "Synchronization of nonlinear circuits in dynamic electrical networks with general topologies," *IEEE Trans. Circuits Syst. I: Regular Papers*, vol. 61, no. 9, pp. 2677–2690, Sep. 2014.
- [23] I. Sowa, T. T. Tran, T. Heins, D. Raisz, and A. Monti, "An average consensus algorithm for seamless synchronization of Andronov-Hopf oscillator based multi-bus microgrids," *IEEE Access*, vol. 9, pp. 90441–90454, 2021.
- [24] M. C. Chandorkar, D. M. Divan, and R. Adapa, "Control of parallel connected inverters in standalone AC supply systems," *IEEE Trans. Ind. Appl.*, vol. 29, no. 1, pp. 136–143, Jan. 1993.
- [25] Z. Shi, J. Li, H. I. Nurdin, and J. E. Fletcher, "Comparison of virtual oscillator and droop controlled islanded three-phase microgrids," *IEEE Trans. Energy Convers.*, vol. 34, no. 4, pp. 1769–1780, Dec. 2019.
- [26] B. Johnson, M. Rodriguez, M. Sinha, and S. Dhople, "Comparison of virtual oscillator and droop control," in *Proc. Workshop Control Model. Power Electron.*, 2017, pp. 1–6.
- [27] J. Hu and H. Ma, "Synchronization of the carrier wave of parallel three-phase inverters with virtual oscillator control," *IEEE Trans. Power Electron.*, vol. 32, no. 10, pp. 7998–8007, Oct. 2017.
- [28] M. Sinha, J. Poon, B. Johnson, M. Rodriguez, and S. Dhople, "Decentralized interleaving of parallel-connected buck converters," *IEEE Trans. Power Electron.*, vol. 34, no. 5, pp. 4993–5006, May 2019.
- [29] M. Lu, S. Dutta, and B. Johnson, "Self-synchronizing cascaded inverters with virtual oscillator control," *IEEE Trans. Power Electron.*, vol. 37, no. 6, pp. 6424–6436, Jun. 2022.
- [30] P. Achanta, M. Sinha, B. Johnson, S. Dhople, and D. Maksimovic, "Self-synchronizing series-connected inverters," in *Proc. IEEE 19th Workshop Control Model. Power Electron.*, 2018, pp. 1–6.
- [31] S. Strogatz and I. Stewart, "Coupled oscillators and biological synchronization," *Sci. Amer.*, vol. 269, pp. 102–109, Jan. 1994.
- [32] A. Buscarino, L. Fortuna, and M. Frasca, *Essentials of Nonlinear Circuit Dynamics With MATLAB and Laboratory Experiments*. Boca Raton, FL, USA: CRC Press, 2017.
- [33] C. D. Bello, "The nonlinearities for nearly sinusoidal oscillators," *IEEE Trans. Circuits Syst.*, vol. 35, no. 9, pp. 1191–1192, Sep. 1988.
- [34] R. York, "Nonlinear analysis of phase relationships in quasi-optical oscillator arrays," *IEEE Trans. Microw. Theory Techn.*, vol. 41, no. 10, pp. 1799–1809, Oct. 1993.
- [35] B. van der Pol, "On relaxation oscillations," *London, Edinburgh, Dublin Philos. Mag. J. Sci.*, vol. 2, no. 11, pp. 978–992, 1926.
- [36] M. Lu, S. Dutta, V. Purba, S. Dhople, and B. Johnson, "A pre-synchronization strategy for grid-forming virtual oscillator controlled inverters," in *Proc. IEEE Energy Convers. Congr. Expo.*, 2020, pp. 4308–4313.
- [37] H. K. Khalil, *Nonlinear Systems*. Hoboken, NJ, USA: Prentice-Hall, 2002.
- [38] F. Verhulst, *The Poincaré-Lindstedt Method*. Berlin, Germany: Springer, 1996, pp. 122–135.
- [39] A. Buonomo and C. Di Bello, "Asymptotic formulas in nearly sinusoidal nonlinear oscillators," *IEEE Trans. Circuits Syst. I: Fundam. Theory Appl.*, vol. 43, no. 12, pp. 953–963, Dec. 1996.
- [40] B. van der Pol, "The nonlinear theory of electric oscillations," *Proc. Inst. Radio Eng.*, vol. 22, no. 9, pp. 1051–1086, 1934.
- [41] S. Strogatz, *Nonlinear Dynamics and Chaos: With Applications to Physics, Biology, Chemistry and Engineering*. Boulder, CO, USA: Westview Press, 2000.
- [42] O. J. M. Smith, "Spectral output of piecewise linear nonlinearity," *Trans. Amer. Inst. Electric. Eng., Part I: Commun. Electron.*, vol. 78, no. 5, pp. 543–549, 1959.
- [43] A. Andronov, A. Vitt, and S. Khaikin, *Theory of Oscillators. International Series of Monographs in Physics*. Oxford, U.K.: Pergamon Press, 1966, vol. 4.
- [44] B. Johnson, M. Sinha, N. Ainsworth, F. Dörfler, and S. Dhople, "Synthesizing virtual oscillators to control islanded inverters," *IEEE Trans. Power Electron.*, vol. 31, no. 8, pp. 6002–6015, Aug. 2016.
- [45] M. Awal, H. Yu, H. Tu, S. M. Lukic, and I. Husain, "Hierarchical control for virtual oscillator based grid-connected and islanded microgrids," *IEEE Trans. Power Electron.*, vol. 35, no. 1, pp. 988–1001, Jan. 2020.
- [46] L. O. Chua and G. Lin, "Canonical realization of Chua's circuit family," *IEEE Trans. Circuits Syst.*, vol. 37, no. 7, pp. 885–902, Jul. 1990.
- [47] G. F. Franklin, D. J. Powell, and A. Emami-Naeini, *Feedback Control Dynamic Syst.*, 4th ed. Hoboken, NJ, USA: Prentice-Hall, 2001.
- [48] M. Lu, V. Purba, S. Dhople, and B. Johnson, "Comparison of droop control and virtual oscillator control realized by Andronov-Hopf dynamics," in *Proc. 46th Annu. Conf. IEEE Ind. Electron. Soc.*, 2020, pp. 4051–4056.
- [49] M. Lu, G.-S. Seo, M. Sinha, F. Rodriguez, S. Dhople, and B. Johnson, "Adaptation of commercial current-controlled inverters for operation with virtual oscillator control," in *Proc. IEEE Appl. Power Electron. Conf. Expo.*, 2019, pp. 3427–3432.